

**HYDRODYNAMIC CAVITATION ON HIGH RESISTANT
MICROFLUIDIC CHIPS**

by
MOEIN TALEBIAN GEVARI

Submitted to the Graduate School of Engineering and Natural Sciences
in partial fulfilment of
the requirements for the degree of Master of Science

Sabanci University
June 2020

HYDRODYNAMIC CAVITATION ON HIGH RESISTANT
MICROFLUIDIC CHIPS

Approved by:

Prof. Ali Koşar
(Thesis Supervisor)

Dr. Morteza Ghorbani
(Thesis Supervisor)

Dr. Meral Yüce

Prof. Dmitry Grishenkov

Prof. Anna J. Svagan

Date of Approval: June 10, 2020

MOEIN TALEBIAN GEVARI 2020 ©

All Rights Reserved

ABSTRACT

HYDRODYNAMIC CAVITATION ON HIGH RESISTANT MICROFLUIDIC CHIPS

MOEIN TALEBIAN GEVARI

Mechatronics M.A. THESIS, JUNE 2020

Thesis Supervisor: Prof. Ali Koşar & Dr. Morteza Ghorbani

Keywords: Microfluidics, Hydrodynamic Cavitation, Energy Harvesting, Bacteria
Inactivation, Cavitation on a Chip

Cavitation is one of the phase change phenomena, which occurs as a result of a sharp static pressure drop in a fluidic system. The required pressure drop could be obtained either by acoustic wave propagation, known as acoustic cavitation, or by hydrodynamic pressure drop, known as hydrodynamic cavitation. There are different parameters affecting flow patterns in hydrodynamic cavitation such as geometry of the flow path, thermophysical properties of the working fluid, and roughness elements. In this thesis, high pressure resistive microfluidic devices are fabricated and tested at high inlet pressures. The flow behavior is characterized using cavitation number, Reynolds number, and cavitation flowrate. Different working fluids such as ethanol, PBS, and PFC5 droplets suspension in water are used and the performances of the devices are compared with the case of water. The effect of different lateral wall roughness elements on the flow pattern is studied and the general geometry of the devices is optimized. In addition, applications of hydrodynamic cavitation are considered. The energy harvesting application of hydrodynamic cavitation is implemented and the amount of the possible power generation of the microfluidic devices in the case of coupling with $\mu-TEGs$ is analytically investigated. Finally, the bacteria removal performances of the microfluidic devices are assessed. The advantages of the designed and fabricated microfluidic devices are presented and explored as well.

ÖZET

YÜKSEK DİRENÇLİ MİKRO AKIŞKAN ÇİPLERDE HİDRODİNAMİK KAVİTASYON

MOEIN TALEBIAN GEVARI

Mekatronik Mühendisliği YÜKSEK LİSANS TEZİ, HAZİRAN 2020

Tez Danışmanı: Prof. Dr. Ali Koşar & Dr. Morteza Ghorbani

Anahtar Kelimeler: Mikroakışkanlar, Hidrodinamik Kaviteasyon, Enerji Depolama,
Bakteri İnaktivasyonu, Çipin Üzerindeki Kaviteasyon

Kaviteasyon, akışkan bir sistemdeki statik basınç kaybının bir sonucu olarak meydana gelen faz değişimidir. Gerekli basınç düşüşü, akustik kaviteasyon olarak bilinen akustik dalga yayılımı veya hidrodinamik kaviteasyon olarak bilinen hidrodinamik basınç düşüşü ile elde edilebilir. Hidrodinamik kaviteasyonda akış düzeni etkileyen, akış yolunun geometrisi, çalışma akışkanının termofiziksel özellikleri ve pürüzlülük elemanları gibi farklı parametreler ele alınabilir. Mevcut akış fiziğini tezde, yüksek basınca dayanıklı mikroakışkan cihazlar imal edilmiş ve yüksek giriş basınçlarında test edilmiştir. Akış davranışı, kaviteasyon sayısı, Reynolds sayısı ve kaviteasyon akış hızı kullanılarak karakterize edilmişlerdir. Etanol, PBS ve Suda PFC5 damlacıkları süspansiyonu gibi farklı çalışma akışkanları, kullanılmış ve cihazların performansı suyla karşılaştırılmıştır. Farklı yanal duvar pürüzlülük elemanlarının akış paterni üzerindeki etkisi incelenmiş ve cihazların genel geometrisi optimize edilmiştir. Hidrodinamik kaviteasyonun enerji hasat uygulaması analiz edilip ve $\mu - TEG$ 'lerle birleştirilmesi durumunda mikroakışkan cihazların olası güç üretim miktarı analitik olarak araştırılmıştır. Son olarak, mikroakışkan cihazların bakteri yoketme performansı incelenmiştir. Tasarlanan ve üretilen ve üretilmiş mikroakışkan cihazların avantajları da açıkça belirtilmiştir.

ACKNOWLEDGEMENTS

This thesis is dedicated to my beloved family who supported me during the process. Overcoming this academic ordeal was impossible if I did not have the privilege of their mental and physical support.

A especial thanks goes to my dear Sabanci friends who were more than friends to me during the past two years especially my best friend, Soroush Niazi, who has been my cheerleader during the past 7 years of his sincere friendship.

My gratitude towards my advisors, Dr. Morteza Ghorbani and Dr. Ali Koşar, is impossible to be expressed in words. They not only taught me academic ethics but also the fundamentals of being a better scientist to make the world a better place to live. I wish them the best of luck in their career and hope our academic paths cross again someday in future.

This study was supported by TUBITAK (The Scientific and Technological Research Council of Turkey) Support Program for Scientific and Technological Research Project Grant, 217M869 and the Sabanci University Internal Project Grant, Grant No. I.A.CF-18-01877. Equipment utilization support from Sabanci University Nanotechnology Research and Applications Center (SUNUM) is gratefully appreciated.

This thesis is dedicated to my beloved family

TABLE OF CONTENTS

LIST OF TABLES	x
LIST OF FIGURES	xi
LIST OF ABBREVIATIONS	xiii
1. Chapter one: Introduction	1
2. Chapter two: Microfluidic device fabrication and experimental setup	17
2.1. Microfluidic device configuration	17
2.2. Microfabrication process flow	19
2.3. Experimental setup design and assembly	21
2.4. Experimental procedure	23
3. Chapter three: Results and Discussion	24
3.1. Optimization and characterization of the microfluidic devices	24
3.1.1. Lateral roughness element effect on the working fluid behaviour	25
3.1.2. Results and Discussion	27
3.1.2.1. Phase One: Initial Design and Analysis	28
3.1.2.2. Phase Two: Wall Roughness	29
3.1.2.3. Phase Three: Working Fluid Change to Ethanol	32
3.1.2.4. Conclusions	36
3.2. Energy harvesting from collapsing bubbles	37
3.2.1. Materials	38
3.2.2. Preparation of CNF-stabilized PFC5 droplets	38
3.2.3. Results and Discussion	38
3.2.3.1. Device Characterization	39
3.2.3.2. Performance evaluation	41
3.2.3.3. Thermoelectric module implementation	47
3.2.3.4. Conclusions	51

3.3. Bacteria deactivation capabilities of hydrodynamic cavitation	52
3.3.1. Bacteria culturing	53
3.3.2. SEM sample preparation	54
3.3.3. Theory	54
3.3.4. Results and discussion	56
3.3.4.1. Water and PBS flow pattern analysis	56
3.3.4.2. Bacteria/PBS suspension flow pattern analysis	60
3.3.4.3. Bacteria deactivation of hydrodynamic cavitation	63
3.3.4.4. Conclusions	65
4. Chapter four: Conclusion	67
4.1. Future Research Directions	69
BIBLIOGRAPHY	70

LIST OF TABLES

Table 2.1. Geometrical parameters of all the tested devices (all the values are in μm except from β which is in degrees)	19
Table 2.2. Uncertainties in experimental parameters	23
Table 3.1. Three design and optimization phases in this study.	36
Table 3.2. Estimated time between the nucleation and collapse of the bubbles in the devices for the water and droplet-water suspension cases	45
Table 3.3. Potential energy of each control volume for all the devices for both fluids and heat flux to the end wall of the devices	47
Table 3.4. Rate of temperature rise on the end wall in all the devices working for water and droplet-water suspension cases	50
Table 3.5. Thermophysical properties of DI water and PBS.	57

LIST OF FIGURES

Figure 1.1. Different classes of HCRs in the literature Sun et al. [63], Badve et al. [16], Rajoriya et al. [81], Feng et al. [18], and Zupanc et al. [17]	4
Figure 1.2. The facing dimples on the rotational hydrodynamic cavitation reactor used to remove <i>E-coli</i> in Sun et al. [63]	10
Figure 2.1. The configuration of the microfluidic device consisting of three main sections; inlet, nozzle, and extension with wall roughness elements (the total length of roughness elements (L_R) and height of the roughness elements (H_R)).	18
Figure 2.2. Fabrication process flow a) The etched silicon dioxide layer after the first photolithography step, b) the etched silicon dioxide layer after the second photolithography step before removing the photoresist, c) the first deep reactive ion etching of the wafer, d) the second deep reactive ion etching of the microfluidic channel after removing the photoresist layer, e) anodically bonded microfluidic device to the glass (the final product).	20
Figure 2.3. a) Chip holder sandwich with a microfluidic device consisting of three pressure sensors measuring pressure at inlet, nozzle, and extension b) The schematic of the experimental setup including the high pressure nitrogen tank to push the fluid in the system, the fluid container, filter, chip holder sandwich to install the microfluidic device, sterile fluid reservoir to collect the exiting fluid, point light source, high-speed camera, data acquisition system, and proper piping and valves.	22
Figure 3.1. a) Wall roughness elements and bubble b) optical microscopy image of the wall roughness element inside the microchannel.	27
Figure 3.2. The flow patterns of 6 microfluidic devices in the extension section of the devices along with the inlet pressure and cavitation numbers.	29

Figure 3.3. Optimization scenarios and conclusions from the optimum cases in each scenario.	31
Figure 3.4. Design parameters interaction plot showing an intense interaction between the wall roughness elements geometrical dimensions.	32
Figure 3.5. Cavitation flow patterns for devices 4 and 6 (worst cases in the previous phase) working with ethanol.	34
Figure 3.6. Flow rate and cavitation number as a function of Reynolds number	41
Figure 3.7. Bubble size distribution for device 8 for a) water b) PFC5 droplet-water suspension	44
Figure 3.8. Thermal resistance network.	48
Figure 3.9. The performances of three devices a) maximum power generation of the energy harvesting device coupled with the first $\mu-TEG$ [50], b) maximum power generation of the energy harvesting device coupled with the second $\mu-TEG$ [51]	51
Figure 3.10. Cavitation number and flow patterns of the first microfluidic device for the case of water and PBS.	58
Figure 3.11. Reynolds and cavitation numbers and flow patterns of the second and third microfluidic device for the cases of water and PBS.	59
Figure 3.12. SEM imaged of the bacteria before the experiments.	61
Figure 3.13. The flow pattern of the second device working with water and bacteria suspension (merged images from high speed camera).	62
Figure 3.14. The fluid flow pattern of water and bacteria suspension in the third microfluidic device.	63
Figure 3.15. Bacteria colonies on the agar plates exposed to developed cavitating flow at inlet pressure of 4.48 MPa, a) complete growth of the bacteria before the experiments, b) no significant change in the number of colonies after the first cycle of the cavitation (approximately 3 minutes), c) a significant decrease in the number of active colonies after the tenth cycle of the hydrodynamic cavitation (approximately 30 minutes), d) complete deactivation of the bacteria after the fifteenth cycle of the experiments (approximately 45 minutes).	64
Figure 3.16. a) SEM analysis of the sample after the cavitation assay, b) the quantitative data of the bacteria colony number.	65

LIST OF ABBREVIATIONS

<i>μ-TEG</i> Micro Thermoelectric Generator	iv, v, xii, 8, 24, 47, 48, 49, 50, 51, 52, 68
ACR Acoustic Cavitation Reactor	3
AOP Advanced Oxidation Processes	9
CNF Cellulose Nanofibers	6, 37, 38
D-RIE Deep Reactive Ion Etching	6, 20
HAC Hydrodynamic-Acoustic Cavitation	13
HCR Hydrodynamic Cavitation Reactor	xi, 3, 4, 9, 10
LB Luria-Bertani Broth	53, 64
PBS Phosphate Buffer Saline	iv, v, x, xii, 13, 24, 52, 53, 56, 57, 58, 59, 60, 65, 68
PECVD Plasma Enhanced Chemical Vapor Deposition	20
PFC5 Perfluoropentane	iv, v, xii, 6, 37, 38, 40, 43, 44, 45, 50, 68
PVA Poly(Vinyl Alcohol)	7
RIE Reactive Ion Etching	20
ROC Radius of Curvature	5
SEM Scanning Electron Microscopy	xii, 54, 60, 61, 65

1. Chapter one: Introduction

In the second half of the nineteenth century, unusual damage was detected on the ship propellers, which motivated the researchers to make efforts in discovering a phenomenon later named as cavitation. Reynolds was among the first scientists, who tried to explain the reasons for this unusual damage [1]. Parsons was the first person, who acknowledged the key role of vaporization in the caused damage on the ship propellers and performed the first experiments on cavitation in 1906 [2]. Thereafter, many researchers did fundamental studies on cavitation and contributed to the generation of understanding in multi-phase flows. Arndt [3] in 1981 characterized the intensity of cavitation by cavitation number and other non-dimensional numbers. Brennen [4] in 1995 reviewed and explained the physics of nucleation and cavitation in his book.

The destructive effects on the turbomachinery as a result of cavitating flows as well as methods for prevention of cavitation have attracted much attention. Numerical and experimental methods have aided the researchers for these purposes. For instance, Deng et al. [5] developed a numerical model to characterize cavitation in centrifugal pump impellers in transporting water and diesel. They could include the effects of viscosity and surface tension in their proposed model. In another study, Escaler et al. [6] studied cavitating flows in hydro turbines and its negative instability effect on the performance due to the draft tube swirl. They also presented different types of cavitation, namely leading edge cavitation, traveling bubble cavitation, draft tube swirl, inter-blade vortex cavitation, and Von Karman vortex cavitation. The above-mentioned studies proved the destructive potential of the hydrodynamic cavitation which could be utilized in different applications as well.

The advances in small scale bubble generation and the confirmation of the massive energy release upon bubble collapse caused a paradigm shift. Many researchers have already started to exploit the energy release upon collapse of cavitation bubbles in different applications such as energy harvesting [7], water treatment [8, 9], biological applications such as urinary stone treatment [10], food industry [11], and heat transfer [12, 13].

Two major phase change mechanisms are cavitation and boiling. Considering the phase change diagram [14], boiling happens as a result of temperature rise, while cavitation happens as a consequence of pressure drop. The critical value of the local pressure to incept cavitation is considered as the saturated vapor pressure of the working fluid. However, other parameters such as the existence of tensile strength, residence time of the working fluid, presence of contaminant gas, steady viscosity effect, turbulence effect, and many more known and unknown parameters could increase as well as decrease this threshold [4]. The static pressure drop could be obtained using acoustic waves generated by ultrasonic transducers (acoustic cavitation) or by hydrodynamic pressure drop due to the change in the fluid path such as sudden or gradual constrictions known as orifice and venturi and rotations in turbomachinery such as pumps or propellers [13].

Consequently, different cavitation reactors have been designed and tested in the literature. In acoustic cavitation reactors, the power capacity of the transducer and the frequency of the device are important design parameters affecting the working efficiency. Likewise, there are important design parameters such as the number of the holes, diameter of the holes, and total diameter of the plates in orifice plates. Venturi-shaped cavitation reactors, on the other hand, have two main forms of slit and tube. The throat diameter, convergence and divergence angles, and total length of the venturi are of importance in most of the hydrodynamic cavitation reactors.

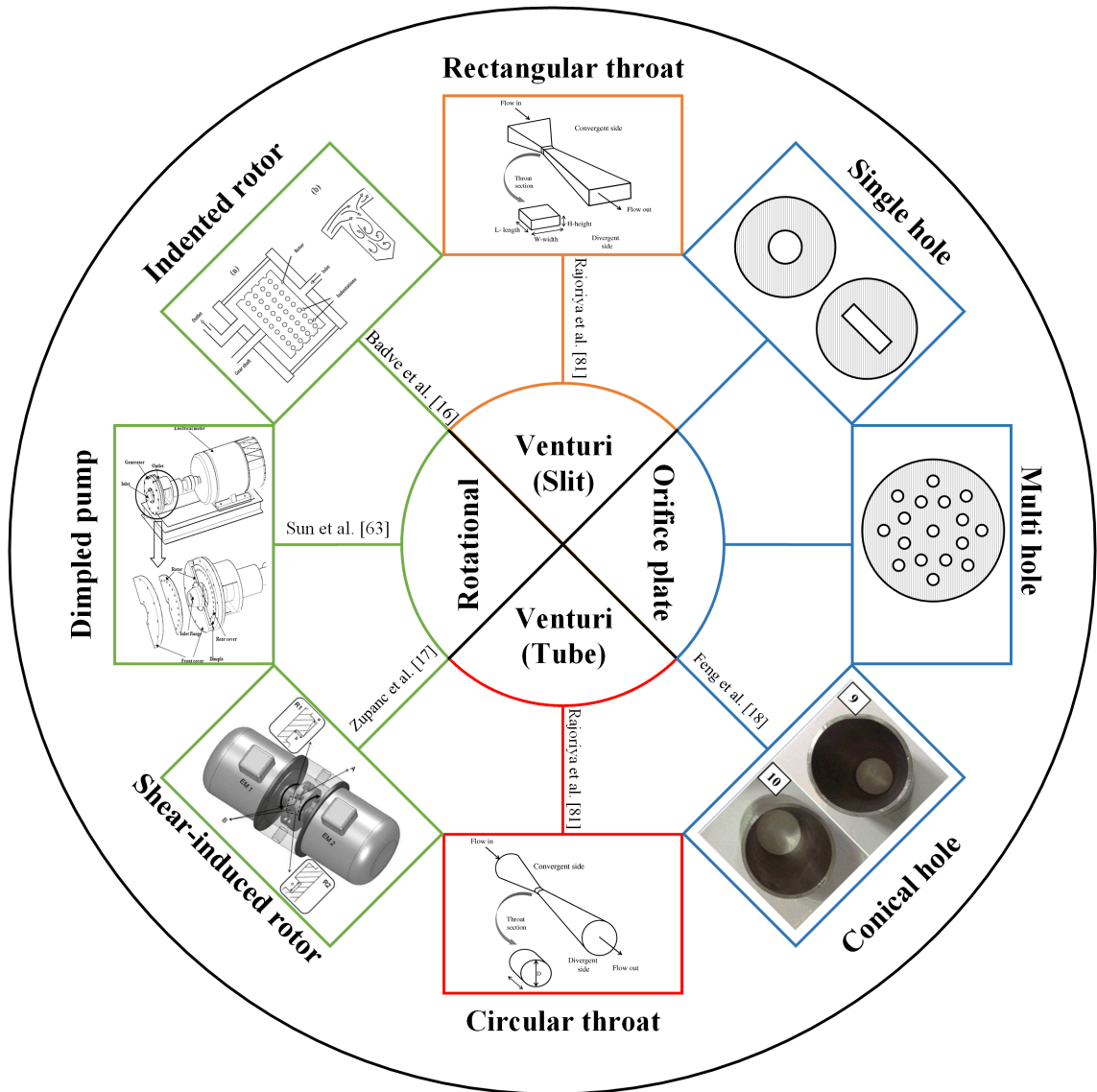
Cavitation is associated with a process involving the nucleation, growth, and implosion of bubbles filled with vapor or gas. Such cavities are generated in a fluid when the static pressure drops below the vapor saturation pressure of the fluid. These bubbles implode violently when encountering with a higher pressure region, resulting in high temperature spots. The local temperature and pressure rises at the cavitation bubble collapse could be as large as 5000 K and 500 atm, respectively [15], which motivates the researchers to study the parametric effects in cavitation generation and to promote such phenomena for the above-mentioned applications.

In addition, the generated aggressive shock waves upon collapse generate active atoms/molecules, which gives rise to chemical reactions. Such outcomes of the bubble collapse constitute a high motivation for researchers to benefit from that in industrial and laboratory applications. The generated energy is capable of accelerating chemical reactions such as oxidation in water treatment. This way, the required temperature rise for this purpose could be decreased. Since the thermal energy of cavitating bubbles is not used to reduce the required thermal energy of water treatment, this is considered as an indirect application of cavitation in this chapter. In other applications, such as heat transfer, the collapsing bubbles could

enhance the rate of heat transfer, which leads to higher efficiency of the devices and processes. In contrary with the previous example, since the generated energy from collapsing bubbles could directly enhance the heat transfer rate of thermal systems, this is considered as direct application of cavitating flow in this chapter. In addition, the energy from cavitation has a good potential in stabilization of nanoparticles in a nanofluid, which could enhance the heat transfer efficiency in processes involving nanoparticles.

Acoustic and hydrodynamic cavitation reactors have been studied in the literature, and there have been significant progresses in this field. In acoustic cavitation reactors, also known as ACR s, the cavitation is initiated as a result of acoustic wave propagation by a transducer in the body of fluid. The ACRs' structure and working mechanism make them hard to scale up to industrial applications. The major reason is the intensity of cavitation, which is reduced with the distance from the horns in the reactor. In addition, the substantial cost of the acoustic wave implementation limits their application in the industry. The inability to treat continuous fluid makes these reactors more suitable for a laboratory scale treatment system rather than an industrial one. Hydrodynamic cavitation reactors (HCRs) on the other hand are available in two main groups: rotational [16, 17] and non-rotational reactors [18]. The rotational HCRs take the advantage of the viscosity of the fluid and their natural static pressure drop upon acceleration to generate cavitating flows for water treatment. Non-rotational HCRs on the other hand uses sudden constriction at the flow path to increase the velocity and to decrease the static pressure of the fluid to generate hydrodynamic cavitation for this purpose. Both kinds of HCRs are capable of being scaled up to use in the industry. However, the non-rotational type is cost effective to be considered as industrial reactors. Consequently, non-rotational HCRs, orifice and venturi types, are typically used to investigate the capability of hydrodynamic cavitation in inactivation of microorganisms and water treatment. Figure (1.1) shows different classes of HCRs reported in the literature during the past years.

Figure 1.1 Different classes of HCRs in the literature Sun et al. [63], Badve et al. [16], Rajoriya et al. [81], Feng et al. [18], and Zupanc et al. [17]



Hydrodynamic cavitation is known to be more energy efficient because of rather simple configuration, low energy requirements, and easier scaling up possibility for industrial applications [19–21]. The stationary sections of these reactors and their easy fabrication process flows increase the popularity and efficiency of these reactors.

Size effects are important in the generation of cavitation phenomenon, and microfluidic systems are suitable platforms for fundamental studies to shed light on microscale cavitation phenomena. The major differences between micro- and macro-scale hydrodynamic cavitation lie in cavitation inception, cavitation hysteresis, and rapid transition to supercavitation flow pattern and choked flow [22, 23]. There are several studies on parameters affecting the generation of cavitation phenomenon. Flow rate (Q_{cav}), cavitation number (σ) [24], Reynold (Re) number, and inception

of cavitation are the crucial parameters, which assist in understanding cavitation phenomenon [24–27]. This has resulted in a number of research articles and patents focusing on both the physics and implementation of this phenomenon.

For instance, Podbevsek et al. [28] fabricated three micro orifices and obtained pressure drop, cavitation number (σ), and flow rate (Q_{cav}), above which cavitation happened. They observed that when the distance between the orifice end and outlet of the chip decreased, an asymmetric behavior could be monitored, and the generated liquid jet was misdirected [29, 30], and other jet flipped to the other side of the channel. The reason for this instability was assumed to be either mechanical effects caused by the high-pressure zone in the outlet or tiny irregularities along the flow path. Mossaz et al. [31] used binary liquid mixtures to study cavitation in two different micro orifices. They reported the cavitation inception for laminar flows at Reynolds numbers of 482 and 520. The reason for this observation with 2-butanol as the working fluid is the small pressure drop in the micro orifice, which depends on the viscosity of the fluid. He et al. [32] studied cavitating flows in a diesel injector nozzle and showed that hydrodynamic cavitation is beneficial in the separation process of sprays. It was concluded that the radius of curvature (ROC) of the entrance hole is the most crucial parameter for a nozzle in affecting internal cavitating flow characteristics. Rudolf et al. [33] investigated hydrodynamic cavitation in single and multi-hole orifices. Their experimental results illustrated that using multi-hole orifices is more effective than single-hole orifices due to their low energy dissipation. Moreover, based on their study, multi-hole orifices lead to a significant drop of loss coefficient in cavitating and non-cavitating regimes. Dong et al. [34] studied the effect of number, arrangement, and ratio of the holes in an orifice plate experimentally. They proved that cavitation number is minimum for a diagonal structure, while it is maximum for the radial structure. Besides, the turbulent kinetic energy shows the maximum value near the edges, and minimum values are seen at the axial lines. Ranade et al. [35] numerically studied the influence of critical geometrical parameters such as orifice thickness, hole inlet sharpness, and wall angle on cavitation flow patterns. According to this study, orifice geometry has a significant influence on cavitation inception. In contrast with the rounded edged orifice, sharp edged orifice generate more intense cavitating flows. In addition, the required pressure for cavitation inception is increased by 30-40 % with angled orifice walls in comparison to a straight throat section, as a result angled orifice walls are undesirable for effective cavitation.

Cavitating flows in micro scale differ from those in macro scale. For instance, experimental investigation of cavitating flows in micro-orifices with a rectangular cross-section showed that the cavitating flow patterns are different from macroscale

orifices. It was demonstrated that incipient and choking cavitation numbers, and cavitating flow patterns of micro-orifices are heavily influenced by the size scale [27]. In this regard, Jin et al. [36] studied the effect of the ratio between the length and diameter of micro-orifices numerically. They reported that the vapor cavity increases with an increase in length to diameter (l/d) ratio, and there exists an optimum value for l/d of a micro-orifice base on both cavitation intensity and flow rate. Ghorbani et al. [37] studied the effect of various lateral wall roughness element geometries in micro orifices fabricated on silicon. They could show that the equilateral triangle roughness elements could increase the intensity of cavitating flows and assisted the development of twin cavities along the channel. In this study, they concluded that small roughness elements and shorter total length raised the intensity. Im et al. [38] emphasized on the importance of nozzle geometry in generating cavitation flows. Carpenter et al. [39] studied the effect of different geometrical cavitation generators on the emulsification of oil in water. They fabricated seven different geometries including both orifice plate and venturi pipe and could prove the direct dependence of geometry on the size of generated droplets. The generated nanoemulsion of mustard oil in water was significantly stable after their experiments under thermal stress and centrifugal condition. They could also demonstrate that hydrodynamic cavitation was 11 times more energy-efficient compared to ultrasonication. Surface topology and geometry of the device are among the most significant parameters, which lead to an increase in the intensity of cavitation flows while causing earlier inception. In this regard, Ghorbani et al. [40] focused on the effects of surface roughness of microfluidic devices on hydrodynamic cavitation. In their study, the roughness was applied using an optimized D-RIE system, while the size of peak-to-peak surface roughness was about $5\ \mu\text{m}$. Their results showed that the roughness on the channel surface lead to intensified cavitating flows in comparison with a smooth channel over the same range of flow rate. They also suggested that longer microchannels were suitable for energy harvesting applications because of the penetration of the emerging twin cavities. In another study, the surface of the microfluidic device was modified by the means of various sizes of silica nanoparticles (CNF-stabilized PFC5) and this surface roughness facilitated the bubbles initiation [41].

Additionally, the thermophysical properties of the working fluid also play a crucial role. Therefore, it is crucial to consider this key parameter in microfluidic devices. Hence, many studies concentrated on these parameters [41, 42]. For example, in the case of a mixture of ethanol and water, choking flow conditions could be obtained at very low cavitation numbers [43]. There are a few studies addressing the application of other working fluids and its effect on the flow pattern. For example, Mossaz et al. [31] reported that the mixture of isopropanol and water could change the

cavitation inception from turbulent regime to laminar regime. Low percentage of isopropanol in water is likely to increase the dynamic viscosity so that cavitation inception corresponding to laminar flow is more easily to be achieved. Hydrodynamic cavitation of water, ethanol and refrigerant liquids in micro venturis was investigated by Mishra et al. [44]. They compared the results of R-123 to those of water and observed that lower surface tension of this fluid enhanced bubble formation. In a subsequent study, different types of liquids were utilized to obtain flow patterns at low upstream pressures for similar devices [43]. A rapid transition from inception to choked flow condition, beyond which the flow rate no longer increased with upstream pressure, was observed. Ghorbani et al. [45, 46] used poly(vinyl alcohol) (PVA) microbubbles in water inside microchannels and transparent cylindrical nozzles with different geometries and compared the results with those of water. They could show that the devices working with PVA had lower cavitation number in comparison with water under the same working conditions. The experimental results from this study also demonstrated that the impact pressure upon bubble collapse was more for the case of PVA. Accordingly, PVA suspensions result in more intensified cavitating flows compared to the reference fluids. Li et al. [47] investigated the influence of thermodynamic effects in the evaporation and condensation coefficient of the cavitation model using an accurate model based on the Rayleigh-Plesset equation. They developed a computational fluid dynamics (CFD) model for simulation of two airfoil cavitation. Their results indicated that the fluid temperature had an effect on the cavitation intensity around the hydrofoil, and the cavitation became more intensive with the increase in the temperature.

All the above mentioned studies would have a larger impact when they could be implemented to industrial or clinical applications. Moreover, controlling the mentioned parameters helped researchers to develop microfluidic devices capable of generating intensified cavitating flows while decreasing the required energy for achieving the supercavitation flow pattern [45]. As a result, large amount of energy could be generated from a small scale cavitation phenomenon, which could potentially fulfill personal energy needs in an environmental friendly fashion.

Growths in energy demand, climate change concerns, and polluted gas emission have pushed the humanity toward clean energy and energy harvesting, thereby minimizing fossil fuel consumption. During the past years, domestic power generation has gained considerable attention. As reported in the Annual Energy Outlook 2019 [48], the power generation from green resources is projected to increase for 13% by 2050, while a decreasing trend in the coal and nuclear resources is predicted. The major conventional sustainable energy sources are wind, solar, geothermal, and hydroelectric energies. New approaches are vital to secure the increase of the share of green

sources.

The formation of cavitating flows in microfluidic systems leads to high temperature gradients and enhanced thermal effects [49], and thermal energy generation is possible due to bubble collapse on the wall of microfluidic devices [7]. Energy harvesting with hydrodynamic cavitation has attracted considerable attention in recent years. However, only few attempts have been made regarding the design and optimization of cavitation on chip devices for the purpose of energy harvesting. One of the suggested methods to harvest the cavitation energy is coupling with a thermoelectric device. Commercial thermoelectric devices have already been tested with cavitating flows. Ghorbani et al. [7] could harvest a maximum power of 0.35 W from cavitating flows in a short micro orifice with an open loop system. They used four different sizes (152, 256, 504, and 762 μm in diameter) of the micro orifices to generate cavitating flows. They increased the upstream pressure up to 60 bar and observed the flow patterns using a high-speed camera. They also utilized a thermal camera to inspect the temperature rise on the surface, where the flow was targeted. They recorded a 5.7 $^{\circ}\text{C}$ temperature rise at the back of the plate as a result of the collapse of the cavitation bubbles.

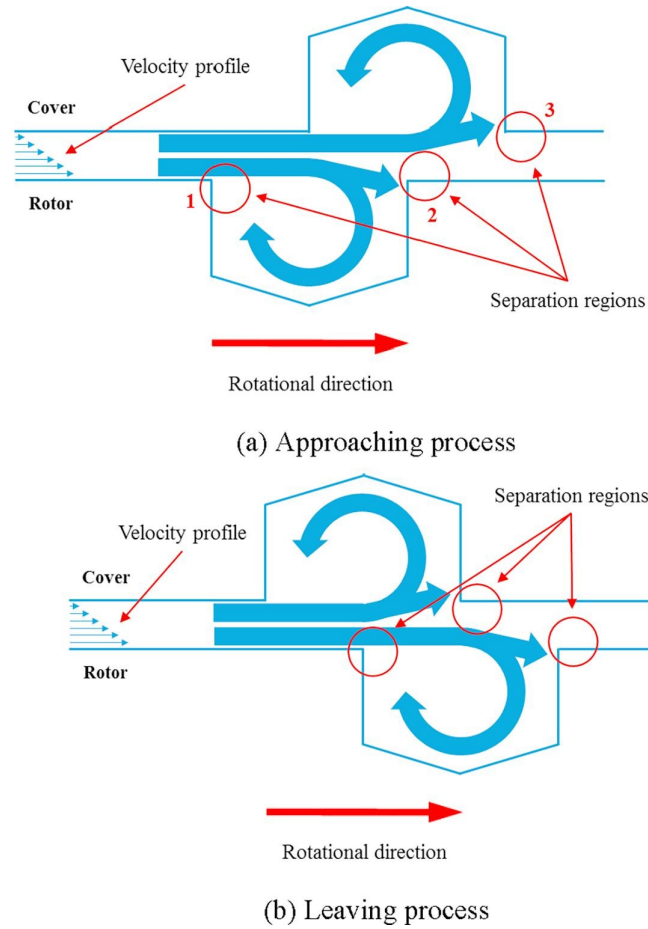
The use of micro thermoelectric generators instead of commercial thermoelectric devices could enhance the amount of the harvested energy. For example, Zhang et al. [50] fabricated a $\mu\text{-TEG}$ using n-type Bi_2Te_3 and p-type Sb_2Te_3 as the thermoelectric material. The internal resistance of their device was reported as 13 Ω , which is one of the major advantages of their device over the other reported devices. They used 127 micro pillars in their device, which lead to a Seebeck coefficient of 116 $\mu\text{V}/\text{K}$. Their experimental results showed that the effective power density of their device at 52.5 $^{\circ}\text{C}$ temperature difference is 9.2 mW/cm^2 . Roth et al. [51] fabricated three electroplated $\mu\text{-TEGs}$ using Bi_2Te_3 , annealed Bi_2Te_3 , Cu, and Sb_xTe_y . They fitted curves to the experimental results and presented two expressions for Seebeck coefficient and internal resistance of the devices. Despite the higher Seebeck coefficient of the thermoelectric with Bi_2Te_3 and Sb_xTe_y , its power generation was the lowest among the other devices. The reason for this result was the higher internal resistance of the thermoelectric generator. On the other hand, annealed Bi_2Te_3 and Cu provided the highest power generation. The maximum generated power in this device was 2338 μW at the temperature difference of 38.64 K. The power density of the best generator in their study was 2.4 mW/cm^2 .

Common methods for water disinfection are divided into physical and chemical methods. Among these methods, heating [52], radiation [53], microwave [54], filtration [55], and plasma [56] could be named as physical ones, while advanced oxidation pro-

cesses (AOPs) such as the implementation of ozone, UV, hydrogen peroxide, or their combination constitute chemical ones, which are widely used especially in textile industry wastewater treatment [57]. The other common methods in water treatment are photocatalysis [58], electrochemical [59], and ionization [60] methods. Acoustic and hydrodynamic cavitation on the other hand are considered as effective methods for water treatment since they are cheaper compared to most of the mentioned methods. Furthermore, no chemical species, which might change the smell, taste, or properties of water, are added to the water in cavitation based methods [61, 62]. The massive energy release of cavitation in the working fluid ($1 - 10^{18} kW/m^3$) has mechanical, thermal, and chemical effects, which are responsible for water treatment and inactivation of microorganisms in water. The generated shock waves, high temperature hot spots, and decomposition of water molecules to active hydrogen and hydroxide radicals with high oxidization capability are the mechanical, thermal, and chemical effects of bubble collapse, respectively. The cavitation application in water treatment decreases or eliminates the need for thermal methods in water treatment plants, which could be considered as the indirect thermal effect of cavitation in this field.

Sun et al. [63] studied the thermal and inactivation effects of hydrodynamic cavitation on wastewater treatment. The HCR used in their study was based on the hydrodynamic heat generator proposed by Kwon et al. [64] in 2013. The suggested cavitation heat generator employed several cone-shaped dimples on the front cover, rotor disk, and rear cover. The dimples facing in the rotational movement of the rotor generate three separation regions, in which the static pressure drops below the critical value thereby triggering cavitation. Figure (1.2) shows the dimples rotating past each other and the generated separation points, at which the static pressure drop happens.

Figure 1.2 The facing dimples on the rotational hydrodynamic cavitation reactor used to remove *E-coli* in Sun et al. [63]



Their experimental results demonstrated that more dimples in the heat generator intensified cavitating flows but more dimples at the same time increased the required flowrate to run the system, which might cause overloading in the motor and possible failure. As a result, the number of dimples is a parameter to be optimized in this category of heat generators.

The thermal effect of cavitating flows is normally considered as a powerful mechanism for water treatment. In this regard, Sun et al. [63] focused on this subject in their study and proved that the thermal effect of hydrodynamic cavitation was the effective mechanism in disinfection. They used simulated affluent water containing *Escherichia Coli* to show the effectiveness of their rotational HCR. According to the results, the flowrate of the working fluid and duration of treatment had no direct effect on disinfection of water. However, the concentration of *E-coli* in water decreased rapidly with temperature, which confirms that the thermal effects remarkably affect, directly and indirectly, the water disinfection performance [65]. Tsolaki et al. [66] in their review article mentioned that temperatures above 40 °C are required to deactivate species in ballast water as thermal treatment. HCRs could increase the

temperature of working fluid up to 70 °C with maximum thermal efficiency of 82.2 % , which makes them ideal for water treatment [63].

Dular et al. [9] extensively investigated the effect of hydrodynamic and acoustic cavitation on the removal of different species from water and wastewater. They used three different hydrodynamic cavitation reactors and presented their experimental results. As a bacteria removal study, they grew artificial *L. Pneumophila* and treated the samples with acoustic cavitation, hydrodynamic supercavitation (corresponding to the minimum cavitation number and maximum cavitation intensity), and developed hydrodynamic cavitation (corresponding to the mid-range cavitation number and grown vapor cavities). The experimental results from 7 cases reported a removal rate of 2 percent per minute for supercavitation, which was four times better than acoustic cavitation and developed hydrodynamic cavitation. In addition, because of fixed pressure nodes in acoustic cavitation reactors, a mechanism should be employed to mix the fluid for better performance, which in turn increases the working cost of these reactors.

Šarc et al. [67] tested whether rapid pressure drop as a result of supercavitation flow pattern could be successful in removing *L. Pneumophila*. They prepared samples of *L. Pneumophila* and treated them in an acoustic cavitation reactor, hydrodynamic cavitation reactor under developed cavitating flow, and supercavitation conditions. According to their results, acoustic cavitation was not effective enough for this bacteria removal process, which is in contrast to the belief in conventional successful application of acoustic cavitation in treatment of other contaminations such as pharmaceuticals. Developed cavitating flow was not also very effective in *L. Pneumophila* removal. However, supercavitation flow regime had good results in the bacteria removal process. To answer their initially proposed question, they put two samples under vacuum condition as well to observe the effect of low pressure boiling on the bacteria. Low pressure boiling was also not successful in damaging the bacteria in the water. This study confirmed that rapid pressure drop as a result of supercavitation exposure was the main removal method for bacteria. An economic feasibility study in this article revealed that the cost of water treatment with hydrodynamic supercavitation was about 0.1 €/m³ which is 3 % of conventional thermal shock method for water treatment. The economic analysis results in this study also evaluated the cost of water treatment for acoustic cavitation and hydrodynamic developed cavitating flow as 40 and 10 €/m³, respectively. The low cost of treatment in hydrodynamic cavitation reactors could be a potential field of more research for the researchers to enhance the efficiency of the systems.

Arrojo et al. [68] studied the effect of hydrodynamic cavitation on *E. Coli* disinfection

tion in water. They did an extensive parametric study and designed a hydrodynamic cavitation chamber consisting of three different multi-orifice plates with the same plate size but different holes in number and size. They utilized three different venturi type cavitation systems as well. Bacteria tended to agglomerate in the medium. Hence, when they were exposed to cavitating flows, the outer crust of the agglomerated bacteria was destroyed, and the concentration of bacteria in the medium increased for a while and then started to decrease with time. The observation in the experiments confirmed that the venturi type cavitator functioned better compared to the multi-orifice plate, which was due to the higher flow rate for a given input power to the system. The comparison between the multi-orifice plates on the other hand confirmed that smaller holes decreased the inertia of the generated micro jet after the plate, which led to a more rapid pressure recovery of the fluid and more frequent introduction of $OH\cdot$ into the fluid. Another significant parameter studied in this study was the effect of discharge pressure on the disinfection rate. The authors could show that the higher discharge pressure for the multi-orifice plate suggested more disinfection rate for the bacteria in water. This conclusion was due to the more aggressive bubble collapse upon discharge pressure increase. On the contrary, increased discharge pressure led to higher static pressure at the recovery region after the plate, which lowered the intensity of the cavitating flow. The lastly studied parameter was the initial concentration of the bacteria in the medium. The obtained results indicated that the rate of inactivation in the orifice plates was reduced with initial concentration, while it remained unchanged for the venturi reactor.

Mezule et al. [69] used a rotational hydrodynamic cavitation reactor to produce bubbles and studied the effect of cavitation on the reproduction potential of *E. Coli*. A treatment as short as 3 minutes and an energy input of 490 W/L could result in 75 % reduction in the reproduction potential of these bacteria, which confirmed the effectiveness of cavitation on bacteria inactivation. Loraine et al. [70] did a parametric study on the effect of hydrodynamic cavitation on removal of different species including *E. Coli*. They used commercial hydrodynamic cavitation reactors and presented the effect of species, nozzle type and pressure, and initial concentration of the microorganism in a batch reactor. Their results showed that the removal rate of *E. Coli* was greatly affected by the nozzle pressure but independent of its geometry.

Cavitation could also be a supporting method to remove microorganisms in water. Karamah et al. [71] discussed the supporting role of hydrodynamic cavitation with ozonation. Their experimental setup consisted of both an ozonator and an orifice plate, which could work in parallel. At first, they tested the effect of cavitation alone on the removal of *E. Coli* and then compared it with ozonation alone.

Accordingly, ozonation was more effective than hydrodynamic cavitation in water treatment. However, their combination as a hybrid system exhibited a different behavior. Cavitation reduced the required dosage of ozone in this process, which lowered the total cost of the disinfection. In addition, the mass transfer of ozone to the working fluid was enhanced due to the small bubbles in the water, which increased the surface area of ozone. The last reason for more effective disinfection was more production of active OH because of cavitating flows.

Su et al. [72] demonstrated for the first time that acoustic cavitation could be effective in removing human enteric viruses such as MS2, FCV-F9, and MNV-1. They employed an acoustic cavitation reactor to treat the viruses suspended in Phosphate-Buffered Saline (PBS) and orange juice. The infectivity of microorganisms in PBS was decreased down to an undetectable level after 30 minutes in the worst case but it took longer for the case in orange juice. They concluded from this observation that food substances could decrease the effectiveness of cavitating bubbles for the treatment. Although Dular et al. [9] did not report the efficiency of their system, they used a hydrodynamic cavitation reactor to inactivate Rotavirus from tap water. Their reactor caused a 75 % reduction in activity of viruses after 400 passes through the venturi shaped reactor. Kosel et al. [73] reported the first hydrodynamic cavitation reactor, whose level of deactivation met the US Environmental Protection Agency's standards (EPA) in removing MS2 from 3 ml of water.

Braeutigam et al. [74] used a hydrodynamic-acoustic cavitation (HAC) reactor to investigate the effect of cavitating bubble collapse on removal of Carbamazepine from water. Their experimental setup consisted of a hydrodynamic cavitation chamber, in which a replaceable orifice was coupled with an ultrasound generator. A heat exchanger elevated the temperature of the working fluid. They did a parametric study on the effect of fluid temperature, initial concentration, diameter of the orifice hole, distance between the orifice hole and sonotrode tip, and other acoustic cavitation parameters. They could report the optimal temperature of 25°C, at which the rate of Carbamazepine conversion peaked and then decreased slightly. They also confirmed the optimum hole diameter of the orifice for Carbamazepine removal, which had already been reported in the literature. At the end, although limited to the small (1 L) working volume considered in that study, they introduced the combination of hydrodynamic cavitation and acoustic cavitation as the best economic and technological method to remove pharmaceuticals from water compared to hydrodynamic cavitation and acoustic cavitation. The HAC reactor removed 96 % of the contamination within 15 minutes. The high efficiency and rapid removal rate of HAC reactors could attract the attention of the researchers to this area.

Petkovsek et al. [75] treated wastewater contaminated with Ibuprofen, Ketoprofen, Carbamazepine, and Diclofenac by a combination of hydrodynamic cavitation, heat treatment, and hydrogen peroxide. They investigated the efficiency of heat treatment and hydrogen peroxide decontamination without hydrodynamic cavitation. The results showed that the combination of these methods with hydrodynamic cavitation dramatically increased the effectiveness. They studied the effect of temperature rise, amount of hydrogen peroxide, and duration of exposure. The increase in time of exposure did not significantly influence the pollution removal in their experiments. In short, cavitation has been proven to be an effective solution for this type of contamination removal, particularly when it is coupled with the other methods such as adding hydrogen peroxide, UV exposure, and heat treatment.

A relatively great portion of the toxic dyes mostly used in textile companies are released into the nature during and after the dyeing process. This number spans around 20-40 % of the dyeing material used in textile industry [76–80]. The textile dyes might cause cancer and genetic problems for human and animals. They are typically among the toxic materials in nature. Common treatment methods such as adsorption, coagulation, membrane separation, and biological processes have not been acknowledged as effective and efficient ways for decolorization of industrial dyes [81]. However, hydrodynamic cavitation in combination with advanced oxidation methods has shown a good performance for this purpose during the past few years. Rajoriya et al. [81] did a comprehensive parametric study for the first time on the effectiveness of hydrodynamic cavitation in combination with different oxidation agents i.e. hydrogen peroxide, Ferrous Sulphate, Oxygen, and Ozone in the removal of reactive blue 13 (RB13). They also studied the geometrical effects of cavitator element on the decolorization rate. All the oxidation agents increased the decolorization rate of cavitating flows through a series of chemical reactions occurring on the interface of gas and liquid phase leading to reactive chemical substances generation. They also demonstrated that there was an optimum amount for each of the mentioned oxidation agents, above which the adverse effects appeared in decolorization. This study included the effect of water pH on decolorization. The experimental results showed that acidic environment was more desirable for this task, which was due to the prevention of $OH\cdot$ recombination by the acid after production in water. On the other hand, the dye was in its molecular form in acidic condition, which drove the hydrophobic dye molecules to the interface of the bubbles, where the concentration of $OH\cdot$ was higher, and more decolorization was consequently achieved. This behavior was reported to be due to the hydrophobic nature of RB13 molecules in this study.

Pesticide pollutions constitute another industrial contamination, which might affect

the environment and hurt human health. They are widely seen in the agricultural industry as insecticides to increase the quality of the products. They are toxic and non-biodegradable and cannot be easily removed from water after common wastewater treatment methods. Gogate et al. [82] studied the effect of hydrodynamic cavitation coupled with advanced oxidation processes on removal of triazophos as one of the toxic and mostly used pesticides. This parametric study displayed the role of inlet pressure, operating pH, and the combined effect of ozonation with cavitation, and Fenton's reagent with cavitation in triazophos removal. The inlet pressure before the orifice plate was varied from 1 to 8 bar, and the optimum inlet pressure, above which the degradation level decreased, was found. The increase in inlet pressure above the optimum pressure caused supercavitation, which led to cavitation cloud presence instead of single cavity. This reduced the intensity of the bubble collapse, which resulted in a decrease in removal rate of the targeted contamination. The pH effect in this investigation confirmed that the extent of degradation under acidic condition was higher than under basic condition. The authors could obtain a removal rate of 96 % with the combination of ozone and hydrodynamic cavitation in this study.

The introduction of foreign microorganisms to an aquatic environment might pose a serious threat to the nature. An unloaded ship fills its containers with ballast water to obtain its stability until it moves to another port and loads its cargo. Since releasing the ballast water into the new area might cause the mentioned problem for the environment, it is necessary to treat the water before discharging it to the new environment. About 10000 different species of microorganisms, phytoplanktons, and zooplanktons can be detected in ballast water tank. The discharge of these microorganisms to the new aquatic environment might trigger biological diversity problems [83], economic issues [84], and human health problems. The potential of cavitation in ballast water treatment has also been investigated by research groups during the past years [18]. In this specific study, the effect of hydrodynamic cavitation generated by three circular orifice plates (single-hole, multi-hole, and conical-hole plates) in deactivation of *Heterosigma akashiwo* in ballast water has been studied. The results showed a 51.12 % deactivation rate by the conical-hole orifice plate for this purpose. The advantage of this system was the low energy consumption for the deactivation of bacteria in ballast water.

Wu et al. [85] showed the capability of a hybrid hydrodynamic cavitation reactor for *microcystis aeruginosa* removal from water. The hydrodynamic cavitation removal efficiency was measured as 20 % after 20 minutes for the best performance case. The combination of ozonation and hydrodynamic cavitation led to a 91 % removal rate. However, the removal rate of ozonation in the absence of cavitating flows was

reported as 24 %, which confirmed the high performance of the hybrid hydrodynamic reactor. Batista et al. [86] investigated hydrodynamic cavitating flows, which were generated in a venturi geometry for scenedesmus removal. They observed an 85 % inactivation effect of cavitating flows after 60 minutes. The fact that this study utilized cavitating flow without any additive suggests that the deactivation rate of cavitating flow depends on the targeted contamination.

In this thesis, high resistive microfluidic devices are fabricated using ordinary clean-room fabrication processes and an experimental setup is designed and assembled to study the physics of high pressure hydrodynamic cavitation in microfluidic devices. The fabricated microfluidic devices can withstand pressures as high as 7.5 MPa without any mechanical failure and can generate high intensity hydrodynamic cavitation. The presence of local vortices in the extension region of the devices increases the working efficiency and intensity of hydrodynamic cavitation. In addition, the effect of wall roughness elements and thermophysical properties of the working fluid on the flow behavior is closely investigated. The final outcome of this thesis is high resistive microfluidic devices capable of intense cavitating flow generation. In addition, the devices are cheap and easy to fabricate in an environmental friendly fashion. For this purpose, the effect of geometrical parameters on the flow pattern is studied and the implementation of wall roughness elements is included in detail. The thermophysical properties of various working fluid are taken into account. Chapter 2 focuses on the microfluidic devices fabrication process flow along with the geometrical features of the designed devices. This section is followed by the experimental setup used in these studies as well as the monitoring methodologies. Chapter 3 presents the results of three experimental studies, discusses the results, and compares the results with the theoretical expectations. Finally, this thesis finishes with the conclusion and significance of the experimental results in industrial and clinical applications.

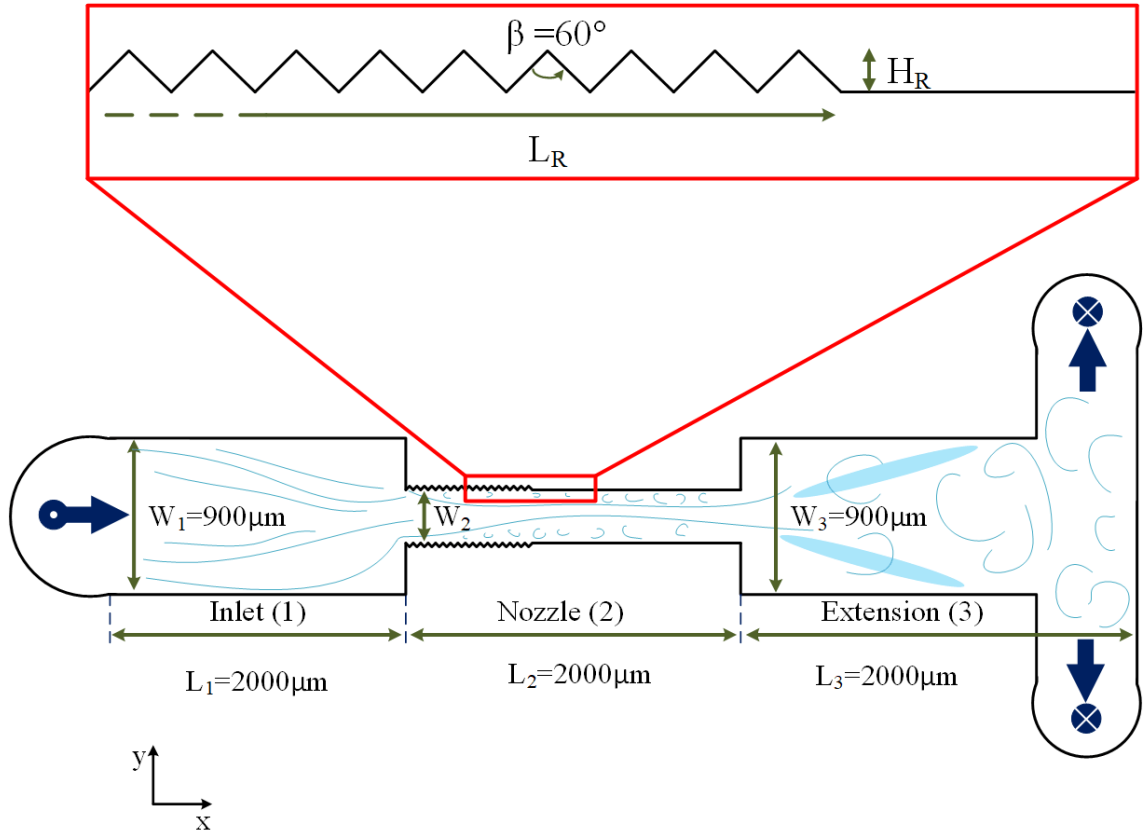
2. Chapter two: Microfluidic device fabrication and experimental setup

In this chapter, the general geometry of the microfluidic devices used during the experiments is presented along with the geometrical parameters, which are altered from device to device for different purposes. The microfabrication methodology is also presented in detail. The experimental setup to install the devices and to propel the high pressure fluid is schematically illustrated. The control parameters and specific measurement techniques are included along with experimental procedures.

2.1 Microfluidic device configuration

The microfluidic device houses a single orifice high pressure hydrodynamic cavitation system etched on a silicon wafer. The general configuration of the fabricated microfluidic device can be seen in Figure (2.1).

Figure 2.1 The configuration of the microfluidic device consisting of three main sections; inlet, nozzle, and extension with wall roughness elements (the total length of roughness elements (L_R) and height of the roughness elements (H_R)).



The microfluidic device is divided in three main sections, namely, inlet, nozzle, and extension. The length of all three sections is $2000 \mu\text{m}$. As a result, the total length of the microfluidic device is $6000 \mu\text{m}$ for all the fabricated microfluidic devices. Three short pressure measurement channels are implemented in the design of the microfluidic devices that the fluid can follow and enter the installed pressure gauges on the experimental setup; before the entrance of the restrictive element, vena contracta (VC), and entrance of the extended channel (5VC-8VC) [87]. The static pressure of the fluid is measured, and the corresponding data points are acquired.

The working fluid enters the inlet perpendicularly and follows the geometry of the microfluidic device after a 90° rotation. The relatively small cross sectional area of the microchannel section provides the sudden pressure drop of the working fluid, which triggers cavitation. In some cases, macroscopic engineered lateral wall roughness elements are embedded on the walls of the nozzle with different total length and height in equilateral triangular shapes. An extension chamber is located downstream so that the fluid could recover its pressure loss, and the bubble collapse is facilitated. Finally, the fluid exits the microfluidic device from two outlets after a

90° rotation. Eleven configurations were fabricated with different geometrical parameters of roughness elements. The width of the inlet and extension are kept the same (900 μm), while the width of the nozzle varies from case to case. The hydraulic diameters ($D_h = 4A_c/P$, A_c and P being the cross-sectional area and wetted perimeter, respectively) of all the cases along with the length are also calculated. Geometrical design parameters of all the devices are listed in Table (2.1).

Table 2.1 Geometrical parameters of all the tested devices (all the values are in μm except from β which is in degrees)

	$L_1 = L_2 = L_3$	$W_1 = W_3$	W_2	D_h	L_R	H_R	β
Device 1	2000	900	152	75	0	0	NA
Device 2	2000	900	152	75	1/3 L_2	0.1 W_2	60°
Device 3	2000	900	152	75	1/2 L_2	0.1 W_2	60°
Device 4	2000	900	152	75	L_2	0.1 W_2	60°
Device 5	2000	900	152	75	1/3 L_2	0.01 W_2	60°
Device 6	2000	900	152	75	1/2 L_2	0.01 W_2	60°
Device 7	2000	900	152	75	L_2	0.01 W_2	60°
Device 8	2000	900	100	66	1/2 L_2	0.01 W_2	60°
Device 9	2000	900	200	80	1/3 L_2	0.01 W_2	60°
Device 10	2000	900	100	66	L_2	0.01 W_2	60°
Device 11	2000	900	400	88	1/3 L_2	0.01 W_2	60°

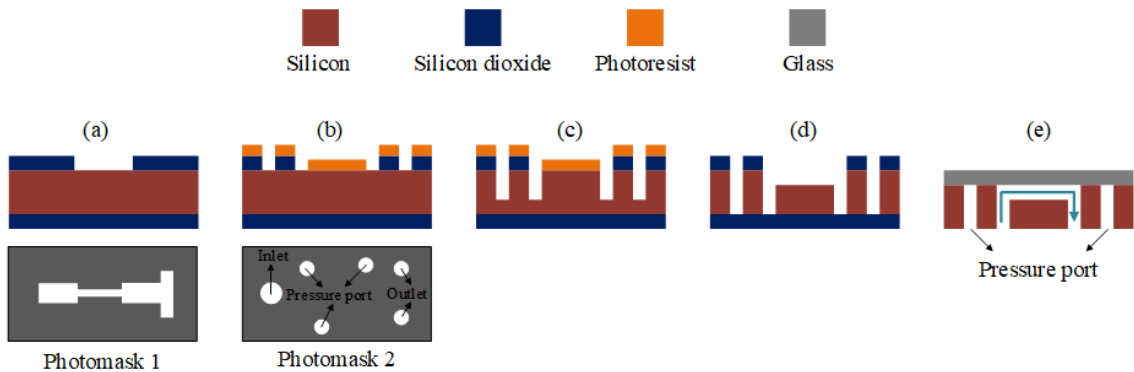
The first microfluidic device has a smooth wall without any roughness element. In the other ten devices, triangular wall roughness elements are achieved in the nozzle section with different total lengths and heights. The total length of the roughness elements is one third, half, and total length of the nozzle (2000 μm). The heights of the elements, on the other hand, are 0.1 and 0.01 of the nozzle width.

2.2 Microfabrication process flow

Since the experiments were performed at high pressures, the microfluidic devices are made of silicon and were bonded to glass to withstand high pressures. Standard microfabrication methods are used to fabricate the devices. All the microfluidic devices were fabricated out of double side polished silicon wafers with a thickness of 380 μm . For this purpose, a 500 nm thick layer of SiO_2 is grown and deposited on both sides of a $\langle 100 \rangle$ silicon wafer using plasma enhanced chemical vapor deposition

(PECVD). A photomask is designed for a photolithography step in the Layout-editor software to make one opening on the substrate corresponding to the whole geometry of the microfluidic device. The pattern of the microfluidic device was transferred on the surface of the substrate using MLA 150 maskless aligner photolithography machine with high resolution on a $2\ \mu\text{m}$ thick layer of photoresist (AZ-ECI) as a positive photoresist. The exposure energy for photolithography was $320\ \text{mJ}/\text{cm}^2$. Reactive ion etching (RIE) of SiO_2 layer and photoresist removal correspond to Figure (2.2-a). The second lithography step with the second photomask followed by a dry etching step similar to the previous step results in Figure (2.2-b). A deep reactive ion etching (D-RIE) process for $330\ \mu\text{m}$ is utilized (Figure (2.2-c)). After the photoresist removal, a further $50\ \mu\text{m}$ deep D-RIE leads to Figure (2.2-d). It is worth mentioning that a $2\ \mu\text{m}$ thick protective layer of Ti and Al is deposited on the backside of the substrate before the last D-RIE so that it survives the applied stress to the sample due to the deep etching. The remaining SiO_2 layer with the protective Al layer on the back is removed. Finally, the substrate is anodically bonded to Borofloat-33 glass after the Piranha cleaning process (Figure (2.2-e)). The resulting microfluidic device is a $50\ \mu\text{m}$ deep single orifice with one inlet and two outlets along with three pressure ports etched on a silicon wafer with glass lead. The total 5 holes in the microfluidic device are $1\ \text{mm}$ in diameter, for which a suitable experimental setup is designed.

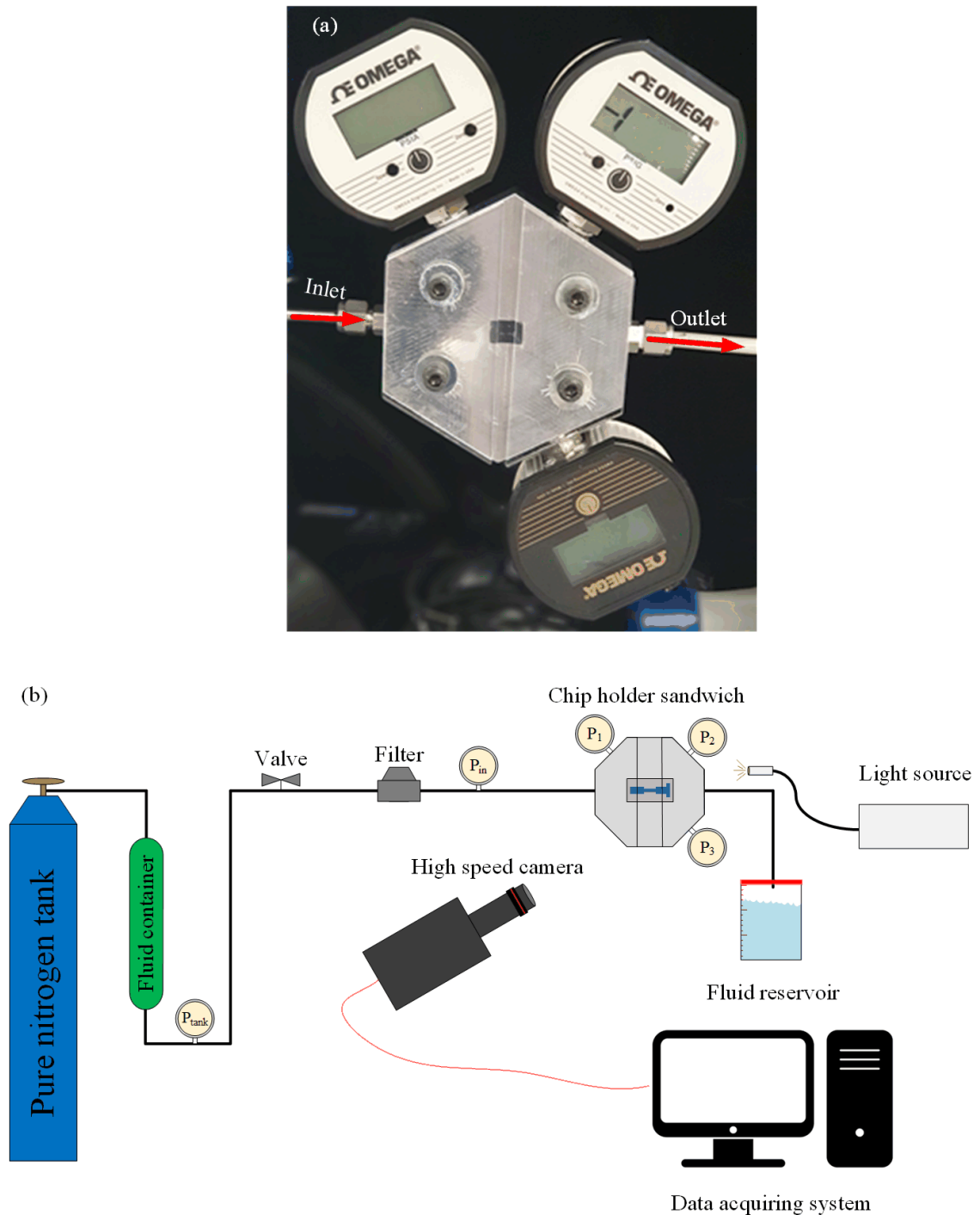
Figure 2.2 Fabrication process flow a) The etched silicon dioxide layer after the first photolithography step, b) the etched silicon dioxide layer after the second photolithography step before removing the photoresist, c) the first deep reactive ion etching of the wafer, d) the second deep reactive ion etching of the microfluidic channel after removing the photoresist layer, e) anodically bonded microfluidic device to the glass (the final product).



2.3 Experimental setup design and assembly

The working fluids are kept in a stainless steel fluid container (Swagelok, Erbusco, Italy), which is connected to a high pressure pure nitrogen tank (Linde Gas, Gabze, Kocaeli, Turkey) from the top, which drives the fluid into the system via proper fittings and stainless steel piping (Swagelok, Erbusco BS, Italy). A needle fine control valve (Swagelok, Erbusco BS, Italy) is installed to control the flow and inlet pressure during the experiments. The microfluidic device is installed and sandwiched on a homemade aluminum package, which facilitated flow visualization. The homemade package consisted of one inlet, which is connected to the fluid container and one outlet, where the fluid exiting the microfluidic device could leave the system. Three pressure sensors (Omega, USA with accuracy value of $\pm 0.25\%$ and the range of up to 3000 psi) are installed to measure P_1 , P_2 , and P_3 (Figure (2.3)). Micro O-rings and tight connections are used to avoid any leakage in the system. A double-shutter CMOS high-speed camera (Phantom v310, with a resolution of 1280×800 pixels, with a pixel size of 0.02 mm along with a macro camera lens (type K2 DistaMax), with the focal length of 50 mm and f-number of 1.2) is used to record the flow patterns during the experiments. The package is installed at 20 cm distance from the camera so that it would be in the focal area. A point halogen light source is used to provide the required background light for better visualization of the flow patterns. The volume flow rate of the system (as measured for each data point and the velocity of the working fluid inside the microfluidic device by dividing a reference volume of the exiting fluid by the elapsed time for this volume to leave the system) is utilized for Reynolds and cavitation numbers calculation. Figure (2.3-b) shows the schematic of the experimental setup.

Figure 2.3 a) Chip holder sandwich with a microfluidic device consisting of three pressure sensors measuring pressure at inlet, nozzle, and extension b) The schematic of the experimental setup including the high pressure nitrogen tank to push the fluid in the system, the fluid container, filter, chip holder sandwich to install the microfluidic device, sterile fluid reservoir to collect the exiting fluid, point light source, high-speed camera, data acquisition system, and proper piping and valves.



The uncertainties in experimental parameters are given in Table (2.2). They were provided by the manufacturer's specification sheets or were obtained using the prop-

agation of uncertainty method presented in the study of Kline and McClintock [88].

Table 2.2 Uncertainties in experimental parameters

Uncertainty	Error
Cavitation number	$\pm 6.5\%$
Reynolds number	$\pm 5.7\%$
Flow rate	$\pm 1.4\%$
Pressure drop	$\pm 0.3\%$
Discharge coefficient	$\pm 1.9\%$
Microchannel width	$\pm 0.2 \mu\text{m}$

2.4 Experimental procedure

The working fluid is kept in the fluid container after degassing. The high pressure nitrogen tank is connected to the container from top and pushes the fluid into the system. The working fluid passes through the valves, pressure sensor, and the filter and finally enters the chip holder sandwich. The working fluid could enter the microfluidic device and undergo the hydrodynamic cavitation process and then exit the outlets of the device. Three pressure sensors installed at inlet, nozzle, and extension regions measure the static pressure of the fluidic system and the high speed camera records the flow pattern during the experiments. The volumetric flowrate of the system is measured to calculate the velocity at different inlet pressures. The exiting fluid is collected in the containers and samples are taken for analysis. The collected exiting fluid could be fed to the system again for other cycles.

3. Chapter three: Results and Discussion

In this chapter, three sets of experiments are performed and the results are presented. The experiments are meant to characterize the cavitating flows and measure the capability of hydrodynamic cavitation on chip in energy harvesting and bacteria removal. For this purpose, the first section deals with the implementation of wall roughness elements in the microfluidic device and compares the performance of the devices in 7 different geometries. The effect of thermophysical properties of the working fluid on the flow pattern is also discussed. Ethanol is used as the new working fluid in this section and the flow behavior is compared with deionized water. The second section studies the capability of three fabricated devices in power generation. In this regard, the devices are assumed to be coupled with two μ -TEGs in the literature and the amount of the generated power as a result of the bubble collapse is calculated. The chapter closes with the performance analysis of the devices in bacteria deactivation. *Salmonella typhimurium* bacteria is cultured and added to PBS as the working fluid. The effect of bacteria presence in the working fluid on the flow pattern and the effect of cavitation on the bacteria removal are discussed in this section.

3.1 Optimization and characterization of the microfluidic devices

In this study, the effect of two key factors, namely, working fluid and roughness elements inside the microfluidic device in the design and optimization are investigated. The microfluidic device with a single orifice is fabricated by conventional microfabrication methods (mentioned in Chapter 2). The microfluidic device is tested at different inlet pressures and the cavitating flow patterns are visualized. The performance of the microfluidic device is evaluated, and wall roughness elements are added to the originally fabricated microfluidic device. In microscale systems, since

the surface to volume ratio is sufficiently high, the surface forces such as surface tension dominate the behavior of the fluid in them and become more important than body forces such as gravity. Consequently, surface roughness can affect the fluid flow in microfluidic devices. Furthermore, surface roughness is a vital factor for phase changing flows, where the inception of the secondary phase is from the surface (i.e. boiling, cavitation, condensation). The surface roughness and cavity size are critical factors in bubble nucleation. In phase changing processes, bubble nucleation and bubble departure frequency increase with surface roughness up to a critical size, beyond which surface roughness has no considerable effect on the nucleation process.

Macroscopic engineered triangle roughness elements are introduced to the design of the microfluidic devices on the walls of the constriction area (nozzle) with different dimensions. The effect of these elements on cavitation flow patterns is studied, and the optimum design area is obtained. Changing the working fluid to intensify cavitating flows in the extension area is the last step in optimization. Finally, an optimum design is suggested for microfluidic devices in order to achieve a facile and intensified cavitating flows. The experiments are done on devices 1 through 7 in Chapter 2 (See table (2.1)).

3.1.1 Lateral roughness element effect on the working fluid behaviour

The sudden pressure drop in the microfluidic device initiates homogeneous and heterogeneous nucleation in the system. Homogeneous nucleation happens in the bulk fluid, while heterogeneous nucleation happens on the interface of the solid and liquid, no matter how small the solid body is. It can even happen on an external particle floating in the body of the fluid.

Surface tension (S) or surface energy represents the intermolecular forces preventing void generation in the bulk of fluid. To elaborate briefly on the homogeneous nucleation in the microfluidic devices, surface tension is scaled down to the microscopic value of bubbles with a few micrometers in size [89, 90].

The difference between the interior pressure of a bubble filled with pure vapor (saturation vapor pressure P_{vap}) and the surrounding pressure (P), denoted as (ΔP_C),

would appear as Eq. (3.1), which is an indicator for the tensile strength of the liquid:

$$(3.1) \quad \Delta P_C = P_{vap} - P = \frac{2S}{R_C}$$

When the surrounding pressure P in Eq. (3.1) drops to a level less than $(P_{vap} - 2S/R)$, the bubbles start growing until a critical radius (R_C) and consequently rupture happens. As a result, an amount of energy is needed to overcome the surface tension between the liquid molecules to generate the void. On the other hand, some work is needed to be done on the liquid (as a control volume) to push the molecules out of the void area. The first term on the right hand side of Eq. (3.2) shows the surface tension energy, while the second term stands for the required work on the control volume:

$$(3.2) \quad W_{CR} = 4\pi R_C^2 S - \frac{4}{3}\pi R_C^3 \Delta P_C$$

This equation includes the total energy (W_{CR}), which is needed for the bulk fluid to nucleate homogeneous bubbles. Homogeneous bubbles might be confused with heterogeneous bubbles because there exist external submicron-sized contaminant particles in the liquid facilitating the heterogeneous nucleation. In addition, the contaminant gases in the liquid start to generate bubbles once the pressure drops under a critical value, which might also be confused with homogeneous nucleation of bubbles. As a result, homogeneous bubble nucleation study is rather complicated.

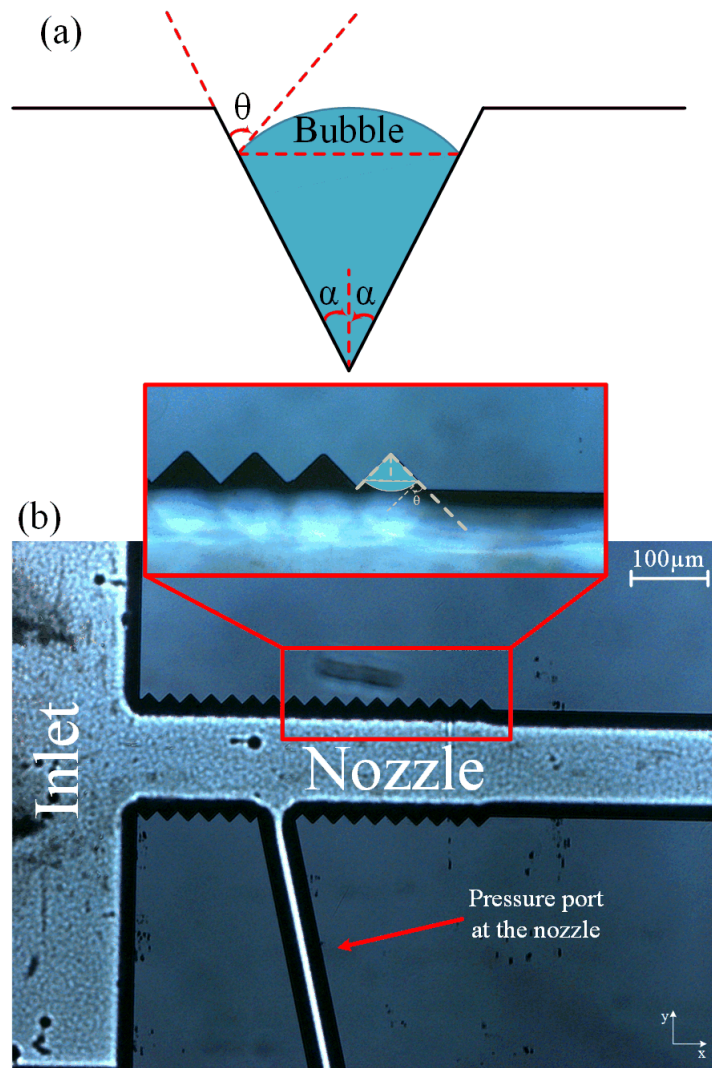
In the heterogeneous nucleation, bubbles form on the interface of solid and liquid. The tensile strength in heterogeneous nucleation of bubbles is expressed as Eq. (3.3):

$$(3.3) \quad \Delta P_C = \frac{2S \sin \theta}{R}$$

where R is the radius of the generated bubble and θ is the contact angle at the interface of gas, liquid, and solid (Figure (3.1-a)). The larger θ reduces the tensile strength of the liquid, which leads to earlier nucleation of the bubbles. Based on the mentioned fact, the fabricated microfluidic device, which did not exhibit any good performance in the first phase of the optimization (no cavitation), is equipped with wall roughness so that it can decrease the inlet pressure, at which heterogeneous

nucleation happens. Figure (3.1-a) shows the wall roughness elements on one of the fabricated microfluidic devices. There are two design parameters in adding roughness elements to the microfluidic device, which are needed to be optimized: the height of the elements (H_R) and total length of the elements (L_R). Six different microfluidic devices are fabricated for this task as shown in Figure (3.1-b).

Figure 3.1 a) Wall roughness elements and bubble b) optical microscopy image of the wall roughness element inside the microchannel.



3.1.2 Results and Discussion

In the fabricated microfluidic devices, the heat energy release upon cavitating bubble collapse is aimed to be collected and converted into electricity by a thermoelectric module installed on the end wall of the extension where bubbles are targeted to. As

a result, reaching to an intense cavitating flow at lower inlet pressures could increase the efficiency of the energy harvesting system. In other words, inception and intensified cavitating flows in the microfluidic device are desired at lower pressures. As a result, lower inception and cavitation development pressures of cavitating flows constitute the optimization goals of this study. The optimization process is performed in three phases, which are explained in the next sections.

3.1.2.1 Phase One: Initial Design and Analysis

The inlet and extension width of the initial design, as mentioned before, is 900 μm , and the width of the nozzle is 152 μm . The widths and lengths of the microfluidic devices are kept constant during the optimization process. Cavitation number, Eq. (3.4), as an indicator to characterize the cavitation phenomena is considered here as an optimization parameter along with the inlet pressure, at which cavitating flow incepts.

$$(3.4) \quad \sigma = \frac{(P - P_{vap})}{0.5\rho V^2}$$

Where ρ is the fluid density and V is the characteristic velocity of the fluid in the microfluidic device calculated at the beginning of the nozzle from the volumetric flow rate of the system.

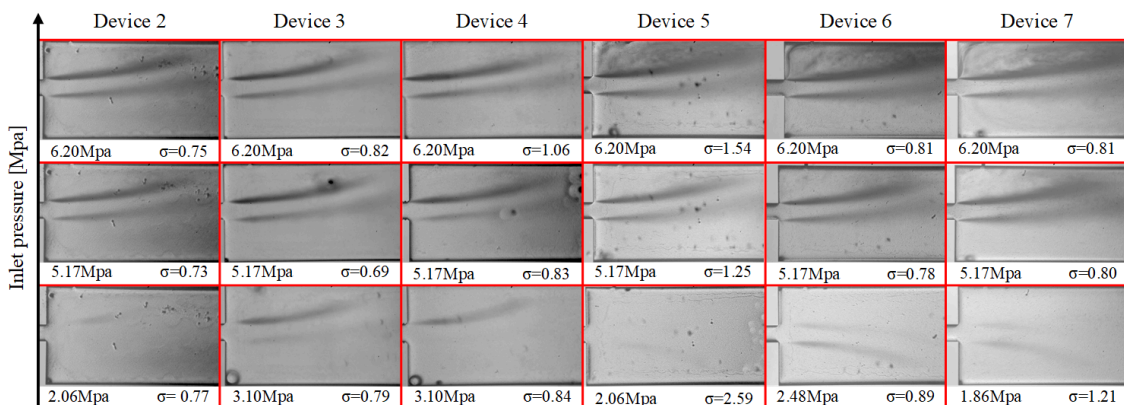
Flow pattern images from the high speed camera during the experiments are also compared at different inlet pressures to indicate the cavitation intensity. Achieving more intensity of the generated cavitating flows is of interest. In addition, reaching developed cavitating flows at lower inlet pressures raises the efficiency in possible applications. In conclusion, more intense cavitating flows at a lower inlet pressure are in favor of this optimization.

The initially designed microfluidic device (device 1) is a plain surface micro orifice with the geometrical features shown in Table (2.1). The device is installed on the chip holder sandwich, and the inlet pressure is gradually increased. The flow patterns are recorded simultaneously during the experiment. For the plain wall configuration, no inception of cavitation is detected over the entire inlet pressure range. The microfluidic devices are durable to inlet pressures of about 7584 kPa. As a result, the microfluidic device needs to be optimized.

3.1.2.2 Phase Two: Wall Roughness

The inlet pressure for each device is increased gradually and kept constant every 350 kPa for a few seconds to make sure that the transient state of the flow pattern has passed and the system is in steady state. The inlet pressure is increased until inception of cavitating flow could be captured by the visualization system on the experimental setup. The cavitation numbers at three different inlet pressures are calculated and compared after the experiments. It should be noted that the inlet pressure is considered as the pressure term in cavitation number Eq. (3.4) and the saturation vapor pressure of water at 20 °C, 2333.14 Pa, is the other pressure term in this equation. The velocity of the fluid is also calculated from the volumetric flow rate of the system at the beginning of the nozzle where velocity is maximum. The density is also 998.2 kg/m^3 in this analysis. Figure (3.2) shows the cavitation number and the inlet pressure of each microfluidic device and the corresponding flow patterns. The cavitation number in microfluidic devices decreases to a point and then increases in all the tests. According to Eq. (3.4), the decrease in the value of the cavitation number is as a result of the velocity increase by increasing the inlet pressure. This trend continues until the microfluidic channel is choked by the flow. Thereafter, the increase in the inlet pressure does not change the velocity of the working fluid. Thus, the cavitation number increases which could be considered as the indicator of the choked flow. The microfluidic devices are tested until this trend is observed for all the cases.

Figure 3.2 The flow patterns of 6 microfluidic devices in the extension section of the devices along with the inlet pressure and cavitation numbers.



As it is shown, the extension inception (the onset of cavitating flow in the extension zone of the microfluidic devices) in device 2 happens at 2.06 MPa, while the same flow pattern is seen at higher inlet pressure of 3.10 MPa in device 4. The difference between these two devices is the total length of the roughness elements. According

to this observation, shorter total length of the roughness elements in device 2 shows better performance as compared to device 4. In addition, the nozzle inception (the inception of cavitating flow at the beginning of the nozzle) happens at 4.13 MPa, while it never happens for device 4. While nozzle inception is not the interest of this study, this can confirm the better performance of device 2 as compared to device 4. On the other hand, the performance of device 3 resembles the performance of device 4 in the extension. However, the nozzle inception was recorded at 5.17 MPa in device 3 which shows a relatively better performance as compared to device 4 with no nozzle inception.

For the first three microfluidic devices (devices 2, 3, and 4), considering the inlet pressure for inception of cavitating flows in the extension section of the microfluidic devices as the optimization goal, it can be concluded that the optimum total length of the wall roughness elements is one third of the total length of the nozzle. Furthermore, the shorter the total length of the lateral roughness elements, the better performance acquired from the device could be considered as the conclusion of this observation.

However, comparing the performance of devices 5, 6, and 7 leads to a different conclusion. The difference between this group of the microfluidic devices with the previous three is the height of the roughness elements which are ten times taller. Device 7 with the longest total length of the roughness elements exhibits the best performance among the tested microfluidic devices. The extension and nozzle inception happened at 1.86 MPa, while the inceptions in the other devices happens at 2.06 MPa and 2.48 MPa, respectively.

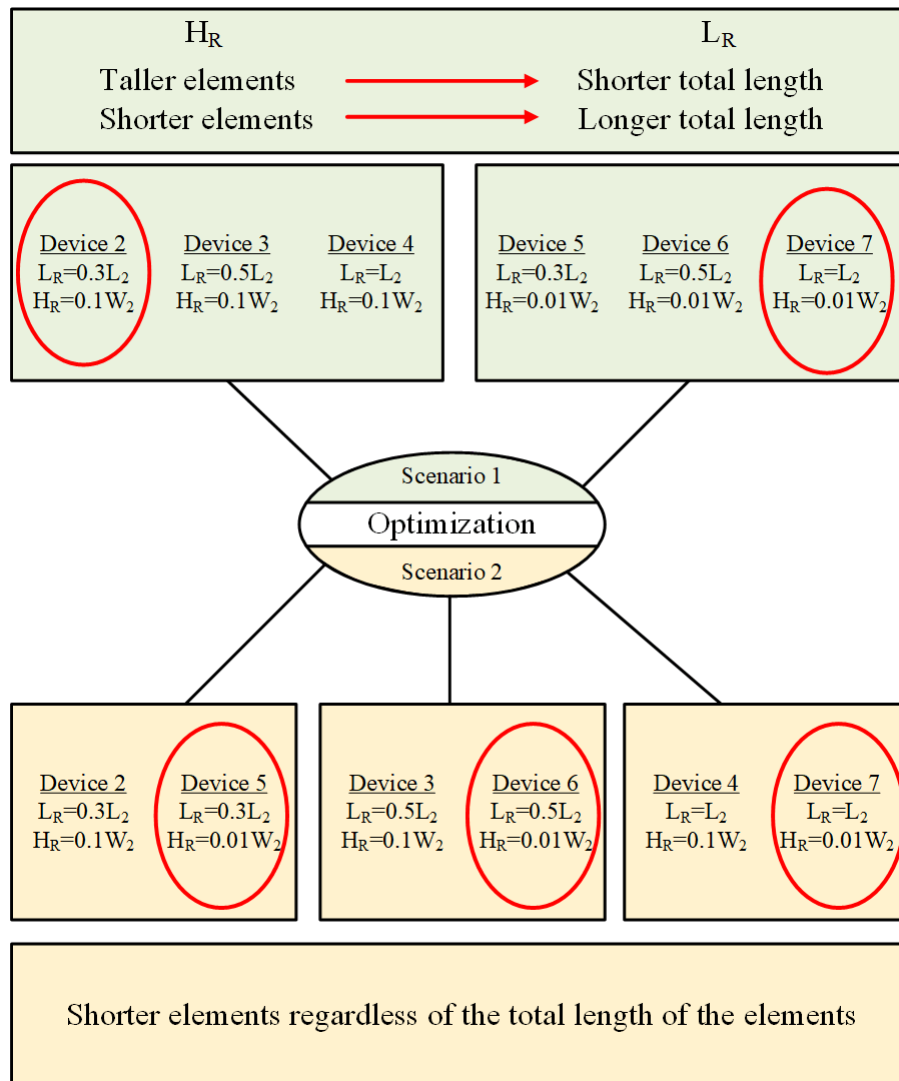
The results of the experimental observations could be interpreted in two scenarios. In the first scenario, the microfluidic devices are divided in to two groups. The members of each group have the same roughness element height but different total length. In the second scenario, on the other hand, the microfluidic devices are divided in three groups in which the length of the roughness elements are the same but the height of them are different.

Based on the first scenario, the shorter total length of roughness elements for the tall elements; device 2, and longer total length for short elements; device 7, are in favor of this optimization process (Figure (3.3)). On the other hand, from the second scenario perspective (roughness height), comparing devices 2 and 5, 3 and 6, 4 and 7, it could be concluded that the shorter elements lead to a better performance of the devices and this conclusion is consistent between all three groups in this scenario. The difference between these pairs of devices lies in the height of the roughness elements. For instance, the roughness height in device 4 is more than in device 7,

and the inception happens at 3.10 MPa, while the inception inlet pressure for device 7 is 1.86 MPa. The other two pairs of the devices follow the same trend in their results. The experimental results for the nozzle inception are also consistent with the extension results.

After both scenarios, devices 4 and 6 could be named as the worst cases between all six microfluidic devices, which will be the interest of the next phase of optimization. The inception of cavitating flows in the extension happens at 3.10 MPa in device 4, and the intensity of cavitating flows in the extension is not very high at the highest inlet pressure of 6.20 MPa (Figure (3.2)). In device 6, on the other hand, the inception happens at 2.48 MPa, and cavitating flows are not intense in the extension at 6.20 MPa (Figure (3.2)).

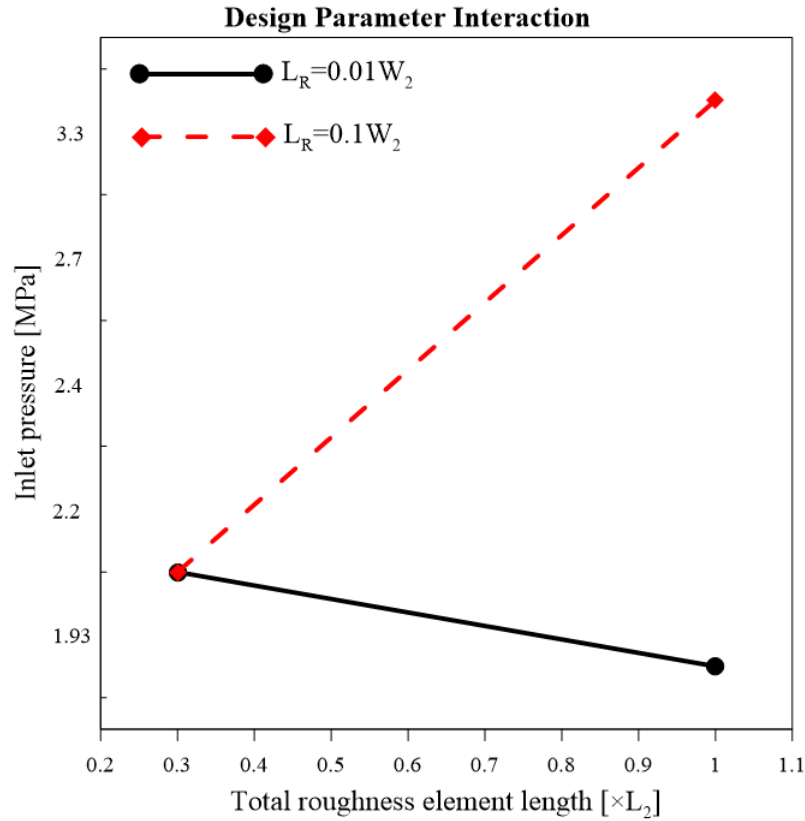
Figure 3.3 Optimization scenarios and conclusions from the optimum cases in each scenario.



The analysis results from the first scenario suggests device 2 as the optimum design,

which has a shorter total length (L_R) and taller roughness elements (H_R) on the wall, whereas the second scenario suggests device 7 as the optimum design, which has the longest total length and the shortest roughness elements. The contradiction between the analysis results show an interaction between the design parameters. A full factorial design on the microfluidic device considering both length and height of the roughness elements shows this interaction in Figure (3.4). The steep angle between the parameter lines in the interaction profile bolsters this claim.

Figure 3.4 Design parameters interaction plot showing an intense interaction between the wall roughness elements geometrical dimensions.



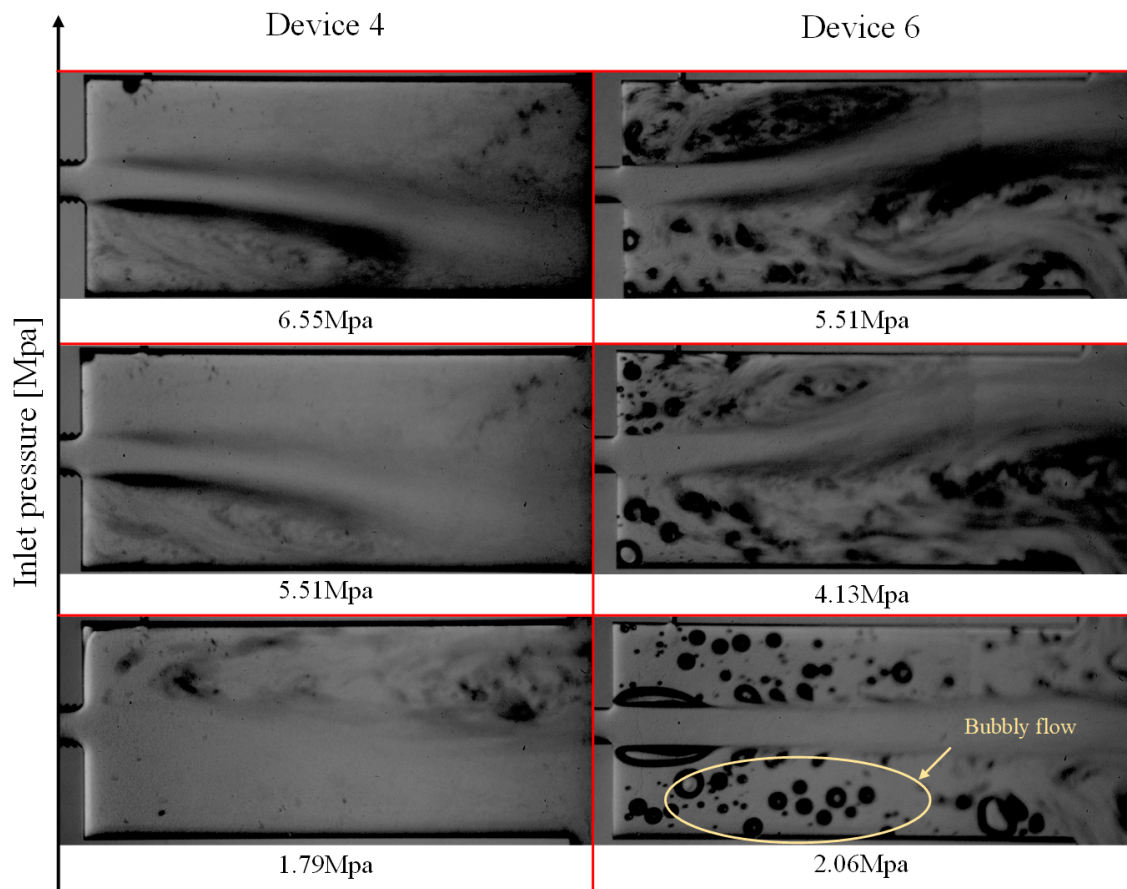
3.1.2.3 Phase Three: Working Fluid Change to Ethanol

It is aimed to use the designed microfluidic device in an energy harvesting system. As a result, a greater number of bubbles in the extension area is desired so that the thermal energy could be harvested from the collapsing bubbles. The fabricated and tested microfluidic devices in the previous phases did not exhibit a good performance in this regard. The extension areas in neither of the cases show an intense presence of cavitating bubbles even at high inlet pressures. As mentioned in Section 2.2, the

tensile strength of the working fluid plays a critical role in bubble generation. Eq. (3.1) shows the tensile strength of the working fluid, and Eq. (3.2) expresses the required energy for to initiate the phase change. Decreasing the surface tension of the working fluid leads to a lower tensile strength and lower energy requirement. The surface tension of water is 72 mN/m at 25°C , while the surface tension for ethanol is 21.78 mN/m at the same temperature. The lower surface tension of ethanol makes it a good candidate for the optimization of the microfluidic devices. 100% ethanol is used to run new sets of tests on the fabricated microfluidic devices from the previous phase of the optimization. In the second phase of the optimization, the worst performance devices in terms of the cavitation inception are devices 4 and 6.

In the case of ethanol as the working fluid, the intensity of cavitating flows in the extension is significantly higher in comparison with the cases with water. The images from the high speed camera show that the number of the bubbles generated in the extension section is significantly higher than that of water at the same inlet pressure. This observation is due to the lower surface tension of ethanol in comparison with water. Apart from the inception pressure difference between ethanol and water, the physics of extension inception is also different. The inception in experiments with water happens gradually with a weak bubble cloud in the extension, while the bubble cloud in the case of ethanol appears suddenly and intensely. In addition, the lower surface tension of ethanol increases its tendency to form bubbly flow rather than bubble cloud, which could be seen in the experiments with water (Figure (3.2)). Figure (3.5) shows cavitating flows in the extension of devices 4 and 6 working with ethanol.

Figure 3.5 Cavitation flow patterns for devices 4 and 6 (worst cases in the previous phase) working with ethanol.



The inception pressure in device 4 working with water is 3103 kPa, while this value drops to 1793 kPa for ethanol. The same trend is visible for device 6 with inception pressure difference of 414 kPa. The reason for this observation could be explained by cavitation flow rate expressed as Eq. (3.5) [91]:

$$(3.5) \quad Q_{cav} = WH \left[\frac{1}{\rho} \frac{P_{out} - P_{vap}}{\frac{W}{wC_d} - 1} \right]^{\frac{1}{2}}$$

where the width of inlet and nozzle are denoted by W and w , respectively and H is the depth of the etched channels in the silicon substrate and C_d is the discharge coefficient of the device in this equation. The flowrate, at which cavitation incepts, is formulated with the geometrical parameters and the thermophysical properties of the working fluid. The vapor pressure of ethanol at $25^\circ C$ is 7.83 kPa, and the density is 789 kg/m^3 , while the vapor pressure and the density of water are 3.17 kPa and 998.2 kg/m^3 , respectively. The higher vapor pressure of ethanol in comparison with water decreases the critical flowrate, at which cavitation incepts, which explains the earlier inception of cavitating flows.

Since the proposed energy harvesting system uses the released heat energy from the collapsing bubbles to generate electricity, ethanol could be nominated as a better working fluid. In this phase of the optimization, the working fluid is changed so that the fluid properties work in favor of this application. Comparing the flow patterns of ethanol and water, more bubbles in the extension are visible for ethanol. On the other hand, the generated bubbly flow and larger bubbles in the extension release more energy upon collapse. Eq. (3.6) can be employed to find the potential energy of the generated bubbles in the microfluidic device:

$$(3.6) \quad E_{pot} = \frac{4}{3}\pi R^3(P_{sat} - P_{vap})$$

where P_{stat} is the static pressure of the surrounding. As can be seen, the potential energy of bubbles (E_{pot}) is in direct relation with the radius of the bubble to the power of three. More than half of this energy is converted to heat after collapse of the bubbles, which is the target of the proposed system [92].

Table (3.1) summarizes and compares the design and optimization phases in this study. The initially designed microfluidic device did not show a good performance in terms of cavitation generation. In Phase II, wall roughness elements with different

heights (H_R) and lengths (L_R) are employed in the nozzle section. The change in the tensile strength of the working fluid facilitates cavitation inception in the extension. The worst cases (performances) in this phase were chosen for the last phase. Ethanol as the working fluid was nominated for Phase III so that the thermophysical differences with water could work in the favor of this optimization goal. The results indicate that the early inception of cavitating flows and its intensification can be achieved by adding lateral roughness elements to the microfluidic devices as the outcome of the second phase of optimization and also intensified by changing the working fluid from water to ethanol. This way, more cavitating bubbles are generated in the extension and goal of the devices, energy harvesting from the collapsing bubbles, could be achieved more conveniently.

Table 3.1 Three design and optimization phases in this study.

	Phase I		Phase II					Phase III		
Optimization Strategy	Initial design	Utilization of wall roughness elements with different height (H_R) and total length (L_R)							Working fluid replacement with ethanol for the worst devices in Phase II	
Device	1	2	3	4	5	6	7	4	6	
Inlet pressure [MPa]	—	2.06	3.10	3.10	2.06	2.48	1.86	1.76	2.06	

3.1.2.4 Conclusions

In this study, single orifice microfluidic devices were designed and fabricated on silicon and were anodically bonded to glass. The fabrication of the devices in silicon could ensure their resistance under high pressure flowing flow without mechanical failure or geometrical deformation. An experimental setup was designed and assembled in order to visualize cavitating flow patterns and to measure pressures at different points. The initially designed microfluidic device was equipped with 6 different lateral wall roughness element configurations, and the performances of the configurations were studied experimentally. Cavitation number is used as the control parameter to make the results consistent during the tests. Two scenarios were considered to analyze the results. In the first scenario, the microfluidic devices were divided in two groups with the same roughness element height but different total length of the roughness elements. The result of the experimental observation showed that for taller roughness elements, shorter total length of them leads to an earlier and more intense cavitating flow in the extension. In addition, for shorter roughness elements, longer total length of the lateral roughness elements is in the favor of the experiments. In the second scenario, on the other hand, the devices were

divided into three groups while in each of them the total length of the roughness elements were the same while the height of them differed. The experimental results confirmed that shorter roughness elements exhibited a better performance regardless of the total length of the roughness elements. Since the conclusions from two scenarios did not match, a parametric effect study was also performed to examine the interactions among the design parameters. In the last phase of optimization, the worst cases from the previous phase were nominated to be tested with ethanol as the working fluid instead of water. The results showed more intense cavitating flow at low inlet pressures for these devices due to the thermophysical differences between both working fluids. The employment of wall roughness elements inside the nozzle could facilitate cavitation flows. Although the initially designed microfluidic device did not generate cavitating bubbles at any inlet pressure, all the secondarily designed and fabricated devices led to cavitating flows in their extension. Ethanol due to its thermophysical properties could considerably enhance the performance of the microfluidic devices and make them ideal devices for energy harvesting applications.

3.2 Energy harvesting from collapsing bubbles

During the past years, there have been few efforts in harvesting energy from cavitation phenomenon. However, there is not any systematic approach for this topic to the best of the author's knowledge. In this study, three different micro orifices (devices 5, 8, and 9 in Chapter 2) are fabricated on a chip and tested under different pressures to observe the cavitation inception, cavitation development, and supercavitation. In addition to water, Perfluoropentane (PFC5) droplets- a new class of cellulose nanofiber-stabilized droplets, where the Oil/Water interface is stabilized by cellulose nanofibers (CNF), are introduced to the system, and their effect on the cavitation phenomenon and energy generation is studied. The fluidic system is assumed to be coupled with two high efficiency micro thermoelectric generators reported in the literature to theoretically estimate the temperature rise in the fluid and the subsequent power generation of the system.

3.2.1 Materials

Perfluoropentane (PFC5, 99%) was purchased from Apollo Scientific (City, U.K.). Bleached sulfite pulp (from Nordic Paper Seffle AB, Sweden) was used in the production of the cationic cellulose nanofibers (CNFs). The CNF suspension (1.32 wt%) were prepared as described previously [93]. The amount of cationic groups, obtained by conductometric titration, was 0.13 mmol per g fiber [94].

3.2.2 Preparation of CNF-stabilized PFC5 droplets

A suspension of CNF (0.28 wt%) was prepared by diluting the stock CNF with MilliQ-water (pH of diluted CNF suspension was 9.5). The CNFs were dispersed with an ultrasonic liquid processor (Sonics Vibracell W750, U.S.). The suspension was treated at an amplitude of 90% for 180 s (using a 1/2" tip) as described previously [93]. The CNFs were ca. 4 nm in width and with a length in the micrometer range. The suspension was brought to room temperature and afterwards 36 g of the (0.28 wt%) CNF suspension was mixed with 1 g of PFC5. The suspension was then processed for another 60 s at an amplitude of 80% under ice-cooling to obtain the stock suspension of CNF-stabilized PFC5 droplets.

3.2.3 Results and Discussion

The results from the experiments are analyzed from flow pattern and energy harvesting perspectives. In section I, the device characterization including the flow behavior along the micro orifices and the effect of the working fluids are presented. In section II, the temperature rises on the end wall of the microchannels are calculated. Finally, the power generation in representative thermoelectric devices coupled with the cavitation system is estimated for all the devices.

3.2.3.1 Device Characterization

There are many parameters affecting the cavitation phenomenon. In order to characterize cavitation, cavitation number (σ) and cavitation flow rate (Q_{cav}) are taken into account. The cavitation number is expressed as in Eq. (3.7):

$$(3.7) \quad \sigma = \frac{(P - P_{vap})}{0.5\rho V^2}$$

The magnitude of this dimensionless number gives valuable information about cavitation intensity.

On the other hand, the cavitation flow rate is the critical flow rate, at which the pressure in the extension becomes equal to the vapor saturation pressure of the fluid. It is an indicator of the relationship between the geometry of the micro orifice and pressure drop. At flow rates more than the cavitation flow rate, cavitation is likely to happen. This parameter is given as in Eq. (3.8):

$$(3.8) \quad Q_{cav} = WH \left[\frac{1}{\rho} \frac{P_{out} - P_{vap}}{\frac{W}{wC_d} - 1} \right]^{\frac{1}{2}}$$

where W and w are the width of the extension and width of microchannel, respectively. H is the height of the channels, and C_c is the contraction coefficient, which is the cross sectional area of vena contracta to the microchannel width.

All the micro orifices were tested under different upstream pressures to capture the cavitation inception, cavitation development, and supercavitation in the micro orifice configurations. The working fluid is water with the density and dynamic viscosity of 998.2 kg/m^3 and $1.002 \text{ mPa}\cdot\text{s}$ at $20 \text{ }^\circ\text{C}$, respectively. The water vapor pressure at this temperature is 2.33 kPa . The inception of the cavitating flow was achieved for the second device (microchannel with hydraulic diameter of $75.2 \text{ }\mu\text{m}$), when the pressure reached 2.96 MPa in case 2, where the flow rate was measured as $454.5 \text{ }\mu\text{L/s}$. Consequently, the upstream velocity of the fluid was 10.1 m/s . Downstream of the microfluidic device, the working fluid enters to the nozzle region. As a result, the velocity of the fluid increases up to 82.23 m/s . The Reynolds number at this section and cavitation number are 12451 and 2.019 , respectively.

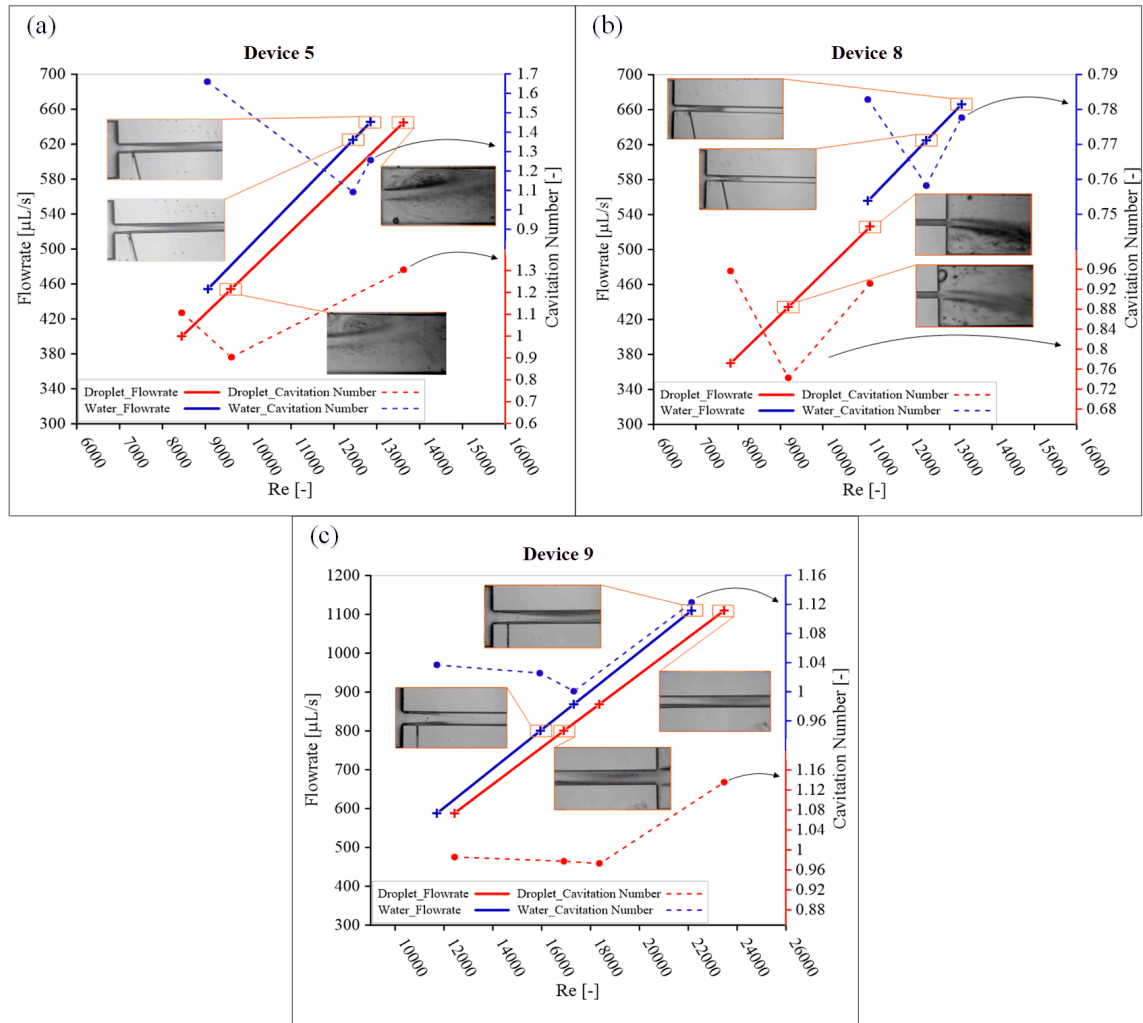
As seen in Eq. (3.8), the cavitation flow rate is dependent on the thermophysical

properties of the working fluid. For this purpose, another working fluid is introduced to the system. The concentration of PFC5 at room temperature is 0.027 vol%, which is diluted for 20 times with distilled water to prepare the suspension for the experiments as the second working fluid. The density and vapor pressure of the new working fluid at 20 °C are 1029.79 kg/m^3 and 6.41 kPa, respectively. As a result, the ratio of the cavitation flow rate of the PFC5 droplets suspension to water is 0.92. Thus, using this working fluid leads to earlier cavitation inception in comparison with the case of pure water. The experimental results agree with this analytical prediction. The pressure at the cavitation inception for the PFC5 droplets suspension is 2.29 MPa.

All the three microfluidic devices are examined at different flow rates with both water and the droplets as the working fluid. The results are shown in Figure (3.6). As can be seen, the inception flow rate of all the cases with the suspension is less than the case with water. Consequently, the Reynolds number, at which the inception occurs, is also less. Thus, it can be calculated that the higher vapor saturation pressure and higher density of the PFC5 droplets can be beneficial in increasing the cavitation intensity and the efficiency of energy harvesting devices. Only in the device 9, this effect is not very considerable, where the dominance of the geometrical dimensions over the properties of the working fluid exists.

The cavitation number is shown in Figure (3.6) (by dashed lines) for each working fluid at different upstream pressures. Increasing the upstream pressure leads to higher velocity of the fluid at the microchannel. Considering Eq. (3.7), the cavitation number decreases until the supercavitation condition. Upon supercavitation, the flow rate cannot be increased anymore, and the flow velocity remains almost constant, which leads to an increase in the cavitation number. This trend can be seen for each of the micro orifices. In most of the cases, the cavitation number for the droplet-water suspension is lower than the pure water case, which is due to lower pressures at the arrival of the inception, supercavitation, and choked flow conditions with PFC5 droplets. The other reason for this observation is the higher density, compressibility, and vapor saturation pressure of the droplets compared to water, which affects the value of cavitation number (Eq. (3.7)).

Figure 3.6 Flow rate and cavitation number as a function of Reynolds number



3.2.3.2 Performance evaluation

As mentioned in Section (3.2.3.1), the growth of the bubbles continues until they reach a critical radius before collapse. The generated bubbles carry a potential energy, which is converted to different kinds of energies such as thermal energy upon the collapse so that this concept could offer an energy source generated with an appropriate energy harvesting device. The generation and development of bubbles have been investigated under both adiabatic and isothermal conditions in the literature [95, 96]. The energy balance of a newly generated bubble by neglecting kinetics and potential energy terms is expressed based on the control volume, which includes the boundary of a bubble nucleating at the beginning of the microchannel

and growing until the beginning of the extension, as Eq. (3.9):

$$(3.9) \quad \Delta Q - P(4\pi R^2 \Delta R) = \left(\frac{4}{3}\pi R^3\right)\rho_g C_{vg} \Delta T$$

where ΔQ is the heat absorbed by the bubble from the surrounding liquid. The second term is the work transferred through the boundaries of the control volume. Since the bubble size grows in this stage, there is not any work entering to the system, but there exists work leaving the system, which explains the negative sign of this term in the energy balance equation. The right-hand side of this equation represents the internal energy change of the gas inside the bubble during the heat transfer period, where R is the mean radius of the bubble, and C_{vg} is the specific heat capacity. Some gases consisting of water vapor and dissolvable gases are trapped inside the generated bubble. The heat transfer through the bubble generates a thermal boundary around the bubble. The thickness of the generated thermal boundary around the bubble is written as Eq. (3.10) [97]:

$$(3.10) \quad d \approx \sqrt{\alpha_l \Delta t}$$

Δt is the characteristic time for heat transfer and α_l is the thermal diffusivity. Here, two scenarios are expected in the comparison between bubble characteristic time for heat transfer and the bubble life time. The first scenario corresponds to the case, where the bubble characteristic time for heat transfer is longer than the bubble life time. In this scenario, the bubble grows and collapses before the heat transfer process could be completed. In the second scenario, the bubble characteristic time for heat transfer is much shorter than the bubble life time, and the bubble lasts long enough to let heat transfer occur before it collapses. In order to investigate the present case, the Fourier's law of heat transfer is applied to the thermal boundary around the bubble while including the definition $\alpha_l = \lambda_l / (\rho_l C_{pl})$ as in Eq. (3.11):

$$(3.11) \quad \Delta Q = -4\pi R^2 \Delta T \sqrt{\lambda_l C_{pl} \rho_l \Delta t}$$

where λ_l is the thermal conductivity. Under the adiabatic condition, ΔQ will be zero in Eq. (3.9). The adiabatic temperature of this process can be then written as

Eq. (3.12):

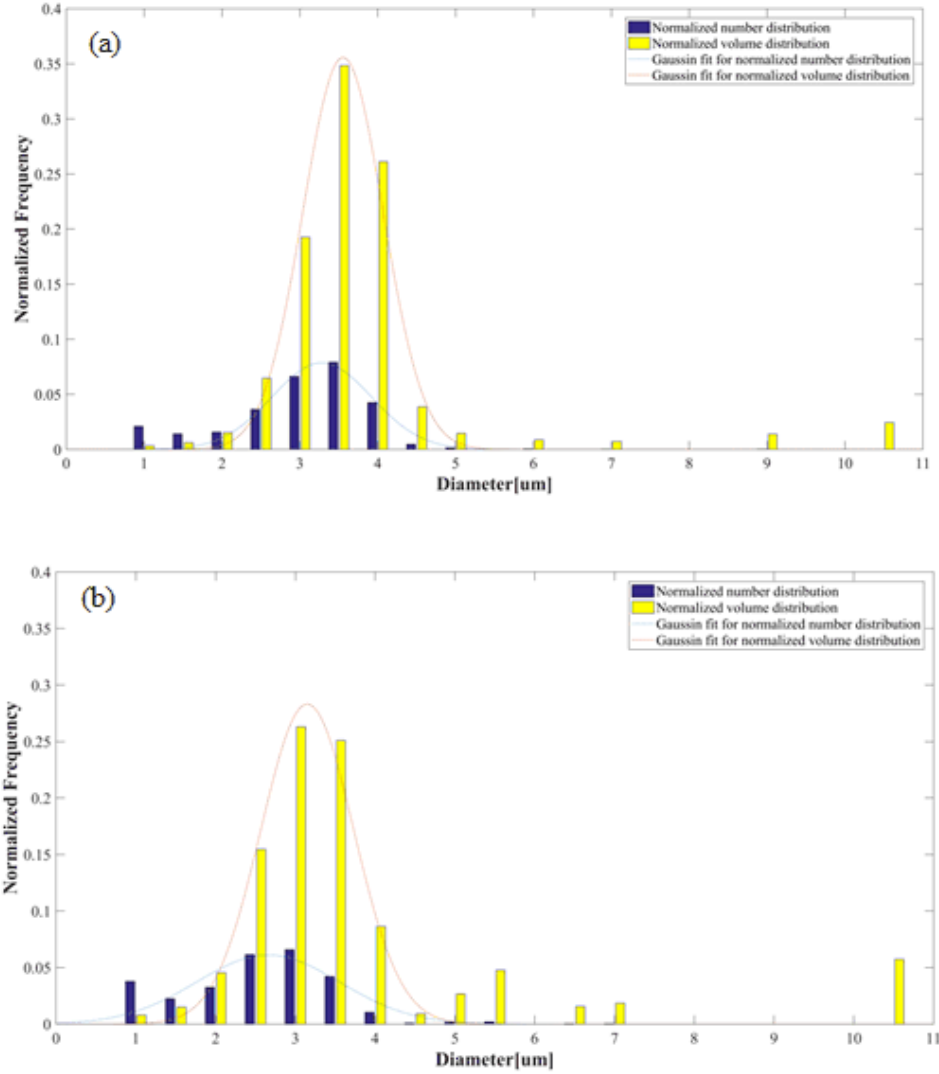
$$(3.12) \quad \Delta T_{ad} = -\frac{3P\Delta R}{R\rho_g C_{vg}}$$

On the other hand, if the process is not adiabatic, and the effect of work in temperature increase is neglected. Then, the Fourier's law can be combined with the energy balance of the bubble, Eq. (3.9), leading to a formulation for characteristic time of heat transfer as in Eq. (3.13):

$$(3.13) \quad \Delta t_r = \frac{(R\rho_g C_{vg})^2}{9\lambda_l C_{pl}\rho_l}$$

In Figure (3.7), bubble size distribution is presented in the light of high-speed camera images taken from the experiments for the working fluid of water at $20^\circ C$ and droplet-water suspension at the same temperature. The bubble diameter was measured with the aid of the ImageJ software (version 1.50b, National institutes of health, USA) to determine the size distribution. The Gaussian distribution is plotted with mean value and standard deviation from the experimental data. An in-house image edge detection *MATLABTM* script (MathWorks Inc., Natick, MA) was implemented to analyze the images and to provide the size and volume distributions. It should be noted that the particle sizes of less than $1\mu m$ have been neglected during the image processing. Accordingly, the mean bubble diameter size is $3.5\mu m$ for water and $3\mu m$ for PFC5 droplet-water suspension. Substituting the bubble size along with the thermo-physical properties of water ($\rho_g = 0.0173\text{ kg}/m^3$, $C_{vg} = 717\text{ J}/kg.K$, $\lambda_l = 0.653\text{ W}/m.K$, $\rho_l = 998.2\text{ kg}/m^3$, and $C_{pl} = 4182\text{ J}/kg.K$) to Eq. (3.13), the characteristic time of heat transfer for a bubble in the device 8 working with water is calculated as $1.92 \times 10^{-11}\mu s$.

Figure 3.7 Bubble size distribution for device 8 for a) water b) PFC5 droplet-water suspension



The distance between the beginning of the microchannel and the end wall at the extension is 4 mm for all three devices. The velocity of the working fluid at supercavitation working with water for the device 8 can be calculated as 82.23 m/s . Consequently, it takes $48.64 \text{ } \mu\text{s}$ for the bubble, which moves at the same velocity as the working fluid to move from the beginning of the microchannel and burst at the end of the extension. Table (3.2) shows the estimated time between bubble nucleation and collapse for all three devices.

Since Δt_r is short compared to the estimated time between the nucleation and collapse of the bubbles, it can be concluded that the dominating mechanism in the development of the cavitating bubbles is the evaporation / condensation (heat

Table 3.2 Estimated time between the nucleation and collapse of the bubbles in the devices for the water and droplet-water suspension cases

Estimated time between nucleation and collapse [μs]		
	Water	PFC5 droplet-water suspension
Device 5	32	38.09
Device 8	48.64	66.88
Device 9	46	36

transfer). While expansion and contraction could be important as well particularly at the beginning and the end of the generation and collapse stages, the isothermal evaporation / condensation plays a more important role in this case. The mentioned discussion can be quantitatively elaborated using the following expression as in Eq. (3.14):

$$(3.14) \quad \Delta T \approx \frac{\Delta T_{ad}}{1 + \sqrt{\frac{\Delta t}{\Delta tr}}}$$

To find the temperature drop in the surrounding fluid due to the bubble generation, the heat flux from the surrounding to the bubble is expressed as in Eq. (3.15):

$$(3.15) \quad \dot{q} = -\lambda_l \frac{T_b - T_\infty}{\sqrt{\alpha_l \Delta t}}$$

The evaporation / condensation heat flux is also stated as in Eq. (3.16):

$$(3.16) \quad \dot{q} = \rho_l L \dot{R}$$

where L is the latent heat of evaporation and \dot{R} is the rate of the bubble growth. By neglecting the initial bubble radius and combining Eqs. (3.15) and (3.16), the temperature difference induced by the bubble generation in the surrounding liquid is obtained as in Eq. (3.17):

$$(3.17) \quad T_b - T_\infty = -\frac{R}{\sqrt{\alpha_l \Delta t}} \frac{\rho_v L}{\rho_l C_{pl}}$$

Because the above estimations are based on the pressure, at which supercavitation appears in the microchannel, the temperature difference of this region is calculated using Eq. (3.17). For this purpose, the bubble radius is assumed to be as large as the width of the microchannel. Thus, the temperature reduction in the working fluid for device 8 is 0.13 K.

As a result, the bubble generation in the microchannel is mostly controlled by evaporation/condensation and the temperature of the working fluid decreases for 0.13 K. The bubbles, which are generated in the microchannel, enter the extension and collapse there. Each bubble carries a potential energy expressed as Eq. (3.18) [91]:

$$(3.18) \quad E_{pot} = \frac{4}{3}\pi R^3(P_{sat} - P_{vap})$$

Accordingly, each bubble in the device 8 carries $2.22 \times 10^{-12} J$ energy for the case of water before the collapse. Half of the potential energy of the cavitating bubbles is converted to heat after collapse [92]. Therefore, finding the number of bubbles entering the extension and collapsing there could reveal an estimation of the heat generation of the cavitating bubbles.

Since the whole volume of the microchannel is occupied with bubbles, when supercavitation happens in the micro orifice, the volume fraction of vapor in the bubble number density calculation can be approximated as one. Multiplying the bubble number density by the vapor occupied volume leads to the number of the bubbles in that control volume Eq. (3.19):

$$(3.19) \quad n = \frac{\alpha}{\frac{4}{3}\pi R^3} \times V_{occ}$$

The control volume, which is being studied for the amount of energy generation is a cuboid with the width and depth of the microchannel and the length of one bubble diameter. The control volume moves with the velocity of the working fluid toward the extension. As a result, V_{occ} in Eq. (3.19) is the volume of this control volume.

The average velocity of the fluid inside the microchannel of device 8 is $82.23 m/s$. Thus, it takes $24.32 \mu s$ to drain one C_V in the extension. Each control volume contains $6.5 \times 10^{-4} \mu J$ of energy delivered to the end wall as heat. Consequently, the area in an optimum distance from the end of the microchannel receives $26.79 \mu W$ of heat for device 8 working with water, which can be converted into electricity by

means of a thermoelectric generator. Table (3.3) shows the potential energy carried by the control volumes in all three devices for water and droplet-water suspension cases as well as the heat flux to the end wall of the microfluidic device.

Table 3.3 Potential energy of each control volume for all the devices for both fluids and heat flux to the end wall of the devices

	Control Volume Potential Energy [μJ]		Heat Flux to the End wall [W/m^2]	
	Water	Droplet-water suspension	Water	Droplet-water suspension
Device 5	11.53×10^{-4}	9.48×10^{-4}	7210	4978
Device 8	13.03×10^{-4}	10.71×10^{-4}	3525	2106.5
Device 9	13.85×10^{-4}	11.38×10^{-4}	3012	3163

Although Table (3.3) shows that the potential energy of the control volumes for the droplet-water suspension case is less than the water case, the energy efficiency is more than the water case. In the case of water, the system needs more input to reach supercavitation compared to the droplet-water suspension case. This is more evident in device 5, where supercavitation happens at 5.9 MPa for water, while the same flow pattern appears at 2.89 MPa for the droplet-water suspension case.

3.2.3.3 Thermoelectric module implementation

Thermoelectric generators are based on the Seebeck effect. Thus, the more the difference between Seebeck coefficient of the p-type and n-type pillars in the device, the more power generation can be obtained. The maximum power generation of the thermoelectric generator device is calculated as $P_{max} = (S\Delta T)^2/4R$. The Seebeck coefficient and resistance are dependent on the temperature rise. The reported results in the literature suggest that they both increase linearly by the temperature increase. Therefore, there exists a tradeoff to be considered in thermoelectric generator design.

Zhang et al.[50] fabricated a μ -TEG device using Bi_2Te_3 as the n-type thermoelectric material and Sb_2Te_3 as the p-type material. Their thermoelectric device consisted of 127 pairs of p-type and n-type materials. The Seebeck coefficient of Bi_2Te_3 with the same electroplating conditions as their project was reported as $-63 \mu\text{V}/\text{K}$ in their previous study [98]. The Seebeck coefficient of the p-type material was also included as $116 \mu\text{V}/\text{K}$. Thus, the total Seebeck coefficient of thermoelectric module will be $S = (116 + 63) \times n = 179n \mu\text{V}/\text{K}$. n is the number of pillars, which is

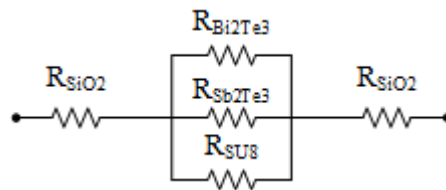
127 in this device. If the top layer of the thermoelectric generator device is made of an ordinary silicon dioxide chip with a thickness of $500 \mu\text{m}$ and the device effective area is $0.65 \times 0.5 \text{ cm}^2$, as reported in Zhang et al.[50], the rate of the temperature rise on this wall is calculated as in Eq. (3.20):

$$(3.20) \quad \dot{Q} = mc \frac{dT}{dt} = \rho V C \frac{dT}{dt}$$

where ρ and C are 2650 kg/m^3 and 680 J/kg.K corresponding to silicon dioxide, respectively. The volume of the field of interest in this equation is the bulk volume of silicon dioxide plate with the area of $0.65 \times 0.5 \text{ cm}^2$, as large as the thermoelectric device effective area. The rate of the temperature rise on this wall is $0.91 \times 10^{-3} \text{ K/s}$. It is important to calculate the temperature rise on an area as large as the end of the extension ($50 \times 900 \mu\text{m}^2$) instead of the effective area of the $\mu\text{-TEG}$ as well. The rate of the temperature rise for device 8 would be 0.66 K/s in this case. As mentioned before, the thermoelectric module should be installed at an optimum distance from the end of the microchannel to harvest more heat energy from the collapsing bubbles. It is worthwhile to mention that the closer the thermoelectric module to the end of the microchannel, the more energy harvesting will be from the collapsing bubbles. The reason is that when the thermoelectric wall is close to the end of the microchannel, the number of the bubbles per unit area is more than the case when the wall is far from this point because less bubbles collapse within an undesirable area before the end wall in this case.

The considered $\mu\text{-TEG}$ consists of four different materials i.e. SiO_2 , SU-8, Sb_2Te_3 , and Bi_2Te_3 . The thermal resistance network approach is utilized to evaluate the heat loss and temperature difference between the hot and cold side across the device. The thermal resistance of the thermoelectric materials and SU-8 are in parallel with each other, and the total thermal resistance of them is considered to be in series with the silicon dioxide top layers (Figure (3.8)).

Figure 3.8 Thermal resistance network.



The thermal conductivity of silicon dioxide, SU-8, Sb_2Te_3 , and Bi_2Te_3 are 1.4, 0.2, 4.7, and 2.9 W/mK , respectively [99, 100]. Considering the conduction heat resistance as $R = L/KA$, (where L is the length, K is the thermal conductivity, and A is the area), the heat transfer rate across the thermoelectric module can be written as Eq. (3.21).

$$(3.21) \quad \dot{Q} = \frac{\Delta T}{R_{tot}}$$

The total thermal resistance of the thermoelectric module is calculated as 22.54 K/W . Consequently, the temperature difference between two sides of the device will be 2.58 K. This shows that if a proper heat sink is used on the cold side of the thermoelectric device, the required temperature difference could be acquired to generate electricity. Under this condition, after a time step of 6 hours, the total temperature rise as a result of the cavitation cloud bubble collapse in device 8 on this wall will be 19.76 $^{\circ}C$.

Although the calculated Seebeck coefficient is 22730 $\mu V/K$, the measured Seebeck coefficient of their device was reported to be 7700 $\mu V/K$ based on the experimental results. This difference was claimed to be due to the fact that the actual temperature difference across the device was smaller than the expected value. In the case of integrating this $\mu - TEG$ device to the present cavitation system with water as the working fluid, the generated voltage will be 156.45 mV. This $\mu - TEG$ has an internal resistance of 13 Ω . As a result, the maximum power generation of the energy harvesting device will be 0.47 mW. The fabricated $\mu - TEG$ has a maximum power generation of 2.9 mW at 52.5 $^{\circ}C$ corresponding to an effective power density of 9.2 mW/cm^2 . The area of the end wall of the devices in the experiments can be found using the width of the microchannel and depth of the channels. As a result, the maximum power generation of device 8 will be 0.7 μW . The cascade design of the cavitation system consists of 10 microfluidic devices working in parallel. For the case, where three cascades work in parallel, a power generation of 0.7 mW could be acquired from the energy harvesting device. This value is twice as big as the value reported in the open loop system, which has been tested before [7]. It is worthwhile to note that the maximum power generation of the energy harvesting system during the time step would be 3.2 mW for device 8 working under supercavitation condition (with water). The same trend is visible for all the devices with both $\mu - TEGs$. This implies that a high performance thermoelectric module coupled with the presented energy harvesting system will lead to substantial power generation.

There are some differences between the power generation for the case of pure water and for the case of droplet-water suspension. First, the diameter of the bubbles in case of droplets is $0.5 \mu\text{m}$ less than water bubbles (Figure (3.7)), which affects the number of bubbles in a control volume and also the amount of the potential energy (Eq. (3.18)). However, the major difference between these cases is the vapor pressure of the water-droplet suspension, which is 4.08 kPa less than pure water. This difference decreases the potential energy of the bubbles. If the same calculations are done as shown above, the rate of the temperature rise on the end wall will be $0.54 \times 10^{-3} \text{ K/s}$, and the output voltage and maximum power generation of the energy harvesting device will be 129.38 mV and 0.32 mW in device 8 for the droplet-water suspension case. Table (3.4) shows the rate of the temperature rise on the end wall (both the area of the thermoelectric module and the actual extension) in all the devices working for both working fluids.

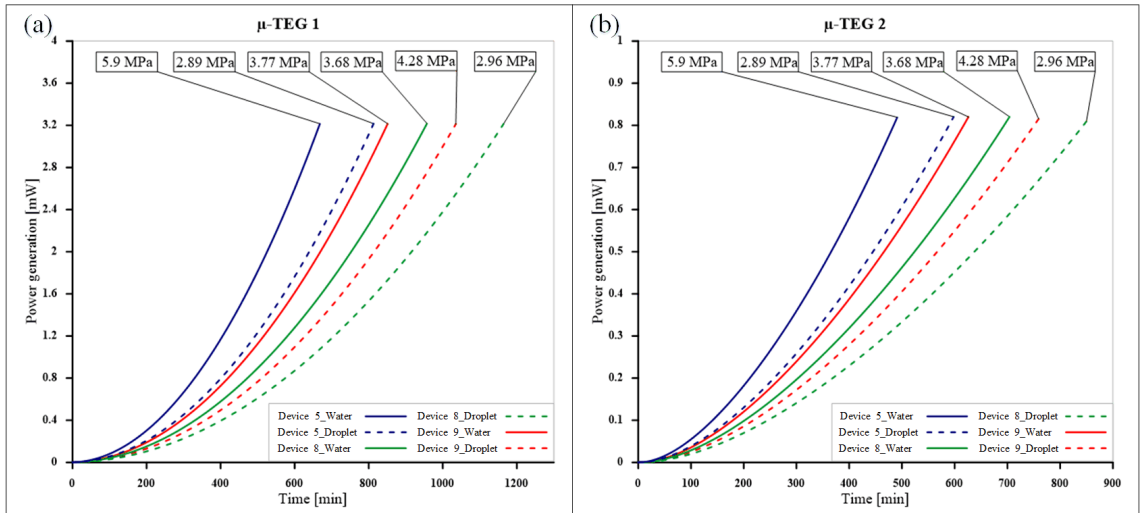
Table 3.4 Rate of temperature rise on the end wall in all the devices working for water and droplet-water suspension cases

	Rate of temperature rise on the end wall [K/s]			
	Water		PFC5 droplet-water suspension	
	Thermoelectric module	Extension	Thermoelectric module	Extension
Device 5	1.23×10^{-3}	0.88	0.84×10^{-3}	0.61
Device 8	0.91×10^{-3}	0.66	0.54×10^{-3}	0.39
Device 9	1.02×10^{-3}	0.74	1.08×10^{-3}	0.78

Roth et al. [51] fabricated a thermoelectric generator using annealed Bi_2Te_3 and copper as the thermoelectric materials. Their experimental results showed a linear dependence between the temperature difference and Seebeck coefficient as well as the electrical resistance and temperature difference. The fitted line to the experimental data resulted in $S(T) = (56.55 + 0.34 T)n \mu\text{V}/K$ and $R(T) = 3.42 + 0.02T \Omega$. They integrated 71 pillars on the generator. As a result, the open circuit voltage and the maximum output power for device 8 working under the supercavitation condition with water as the working fluid are 88.79 mV and 0.26 mW , respectively. They showed that a maximum power generation of 2.33 mW was captured with the temperature difference of $38.64 \text{ }^\circ\text{C}$ across the device corresponding to an effective power density and area of $2.4 \text{ mW}/\text{cm}^2$ and 0.681 cm^2 , respectively. As a result, the power generation of device 8 with end wall area of $(152 \times 50 \mu\text{m}^2)$ being coupled with this $\mu\text{-TEG}$ will be $0.18 \mu\text{W}$. When the cascade configuration is utilized, the whole effective area is covered by the microfluidic device, and the maximum amount of electric power generation could be acquired. Similar to the first $\mu\text{-TEG}$, the thermal resistance network approach is implemented to evaluate the practicality of

this device. The thermal conductivity of copper as the p-type material is taken as 387.6 W/mK . The same calculations are performed for this device, and the total thermal resistance is found as 36.64 K/W . Eq. (3.21) leads to a temperature difference of 8.8 K between the hot and cold sides of the thermoelectric module. The above calculations are valid for the device 8 working under the supercavitation condition. Figure (3.9) displays the power generation of all three devices with both suggested $\mu - TEG$ s. The devices perform better from the energy harvesting point of view for the pure water case. In all the cases, water reaches the maximum allowable power generation of the thermoelectric devices earlier than the water- droplet suspension case. However, it should be noted that the cases working with pure water lead to the supercavitation condition at higher upstream pressures, which affects the efficiency of the whole device. As shown in Figure (3.9-a), the upstream pressures corresponding to the supercavitation in the devices are 36% lower in average for the case of droplet-water.

Figure 3.9 The performances of three devices a) maximum power generation of the energy harvesting device coupled with the first $\mu - TEG$ [50], b) maximum power generation of the energy harvesting device coupled with the second $\mu - TEG$ [51]



3.2.3.4 Conclusions

In this study, three micro orifices were fabricated, and cavitating flow patterns were obtained at different upstream pressures. The experimental and theoretical results showed that the high vapor pressure, density, and compressibility of the water-droplet suspension compared to pure water led to earlier inception of the cavitating flows in all the devices. Supercavitation also occurred earlier for the

droplet-water suspension case. The earlier inception and supercavitation of the devices for the droplet-water suspension case decreased the input energy of the system, which resulted in higher energy efficiency of the whole energy harvesting device. The bubble number density and the potential energy of the bubbles were calculated, and the heat generation as a result of the collapsing bubbles on the end wall of the microchannel was estimated. Two high efficiency μ -TEGs were selected to be coupled with the cavitation system to harvest the energy from the collapsing bubbles. In a time step of about 6 hours, both thermoelectric generators generate their maximum power for the pure water case.

3.3 Bacteria deactivation capabilities of hydrodynamic cavitation

In this section, three microfluidic devices (Devices 5, 10, 11) are fabricated using conventional microfabrication methods on silicon and were bonded to the glass (See Chapter 2). The microfluidic devices withstand high-pressures (up to 8.30 MPa). First, the effect of thermophysical properties of the working fluid (using deionized water and phosphate-buffered saline (PBS)) is studied in the microfluidic devices, and the flow behavior is compared for the case of water and PBS. Cavitation number, Reynolds number, cavitation flow rate, and tensile strength of the working fluid are parameters to analyze the flow behavior. The presence of bacteria, i.e., *S. typhimurium* acts as a solid interface in the working fluid to enhance heterogeneous bubble nucleation. In the last section of this study, a suspension of this bacteria in PBS is prepared and is used as the working fluid. Cavitating flows are visualized in the presence of the bacteria. Finally, the deactivation performance of the device is assessed on one of the microfluidic devices.

As a result, this study focuses on hydrodynamic cavitation from two perspective: first the effects of the thermophysical properties of working fluids on cavitating flows, second the effect of energy release upon bubble collapse on the activity of bacteria. The high deactivation efficiency of the proposed device is also presented and discussed.

3.3.1 Bacteria culturing

Bacteria cultures were prepared from $-80\text{ }^{\circ}\text{C}$ glycerol stocks and used freshly for each assay. *Salmonella enterica* subsp. *enterica* serovar typhimurium (*ATCC*^R14028TM) was cultured in Luria-Bertani Broth (LB) medium (10 g Tryptone, 5 g Yeast extract, 5 g NaCl, Sigma), until the logarithmic growth phase (around 108 CFU/mL) was reached. Bacteria were incubated at $37\text{ }^{\circ}\text{C}$ for 16 h in a shaker at 220 rpm. Growth medium was centrifuged at 5000 rpm for 5 minutes, the supernatant was removed, and the pellet was washed once with PBS and was dispersed in sterile PBS buffer before cavitation experiments. Agar plates were prepared from LB medium supplemented with agar (Sigma) and incubated under similar conditions without shaking.

The bacteria suspension was diluted by 1000 ml PBS to obtain a concentration of 105 CFU/ml before cavitation assay. 100 μl bacteria suspension was kept as a positive control to spread on agar plates. After the cavitation process, collected samples and control samples were diluted to 1:10 with sterile PBS. The diluted bacterial suspensions were spread over the LB agar medium by using sterile glass beads. The plates were placed in an incubator at 37°C overnight, under dark condition. After incubation, the plates were observed for evaluation of the antibacterial effect.

The number of viable bacterial colonies was calculated using the ImageJ software, v.152.a. All Petri dish images were combined in one PNG file and adjusted for brightness/contrast. Every plate image was then converted into 8-bit image, and threshold corrections were applied. Finally, the particle analysis tool was applied to all dishes under identical analysis conditions to obtain the number of colonies per plate.

The PBS/bacteria suspension was collected in sterile biological sample containers upon exiting the microfluidic device and was restored for the next cycle of cavitating flow. Sterile serological pipettes were used to reload the sample into the fluid container in the last part of the experiments (deactivation effects of cavitating flows). The experiments were performed in one shot, and the excess bacteria were kept at 4°C until they were loaded into the system.

3.3.2 SEM sample preparation

Further understanding of bacteria morphology, including size and shape was investigated by Scanning Electron Microscopy (SEM, Zeiss Leo Supra 35 VP, Germany) using an acceleration voltage of 3 kV. In order to provide a sample for SEM analysis, 10 μl of the sample was drop casted on a silicon wafer and was left to dry at room temperature for 3 hours. The sample was coated by gold-palladium alloy to avoid any surface charge of the bacteria and to make the surface homogeneous for image processing.

3.3.3 Theory

In order to characterize hydrodynamic cavitation, the main two parameters are employed: cavitation number and flowrate. Cavitation number is usually used to represent the intensity of cavitating flows in a fluidic system. The cavitation number is expressed as [25]:

$$(3.22) \quad \sigma = \frac{(P - P_{vap})}{0.5\rho V^2}$$

where P is the inlet pressure, P_1 in this study, P_{vap} is the saturation vapor pressure of the working fluid, ρ is the density of the working fluid, and V is the (velocity in the orifice, maximum velocity) of the fluid along the microchannel. P_1 is measured using the pressure sensor in the experimental setup, and P_{vap} and ρ are read from the available look up tables for each working fluid. The volumetric flow rate of the system is measured during the experiments at each inlet pressure, while the value of the velocity is calculated at the beginning of the microchannel (orifice), where the fluid has the maximum velocity.

The inlet pressure is gradually increased during the experiments so that the transition between flow patterns could be observed and accurate images could be recorded by the high speed camera. According to Eq. (3.22), the cavitation number decreases with an increase in the inlet pressure, and the inception occurs either in the microchannel (orifice) or in the extension of the microfluidic devices. The decreasing trend in the cavitation number continues, and the twin cavities emerge and move along the microchannel until supercavitation condition becomes visible. At this

point, the intensity of cavitating flow reaches its maximum in the device. Beyond this point, the flow rate becomes saturated, and the velocity cannot be increased anymore with the inlet pressure. This leads to an increase in the cavitation number, which marks the choked flow condition. Thus, inception, developed cavitating flow, and supercavitation are observed during the experiments.

Cavitation flowrate is the critical flow rate, at which the inception of the cavitating flow is detected in the microfluidic device. Cavitation flowrate is expressed as [27]:

$$(3.23) \quad Q_{cav} = WH \left[\frac{1}{\rho} \frac{P_{out} - P_{vap}}{\frac{W}{wC_d} - 1} \right]^{\frac{1}{2}}$$

where W and w are the width of the inlet and microchannel, respectively. C_d is the discharge coefficient of the device, which was explained and discussed in detail in our previous study [7]. Eq. (3.23) displays the effect of the thermophysical properties of the working fluid on the cavitation flowrate. The saturation vapor pressure directly affects this value, while the density has an adverse relationship with cavitation flowrate, which underlines the importance of the working fluid type on flow behavior.

In addition, tensile strength of the working fluid, which is an indicator for its resistance against forming cavities in the bulk of fluid, could also be used to explain the flow patterns. The tensile strength of the working fluid is given as Eq. (3.24) [10]:

$$(3.24) \quad \Delta P_C = P_{vap} - P = \frac{2S}{R_C}$$

where ΔP_C is the pressure difference between the bubble and the surroundings, S is the surface tension, and R_C is the critical radius of the bubbles before collapsing. The lower tensile strength of the working fluid leads to earlier inception of the cavitating flow. Eq. (3.24) emphasizes on the importance of surface tension of the working fluid on the nucleation of bubbles encountering a low-pressure region.

Besides the mentioned parameters to characterize cavitating flows, Reynolds number, Eq. (3.26), is an important dimensionless number in any fluidic system to

characterize the flow pattern inside the channels [28]:

$$(3.25) \quad Re = \frac{\rho V D}{\mu}$$

where ρ and μ are the density and dynamic viscosity of the working fluid, respectively. The corresponding values are listed in Table (3.5) for water and PBS. On the other hand, V is the velocity of the fluid flow and D_h is the hydraulic diameter of the channel. D_h for rectangular microchannels with side values of a and b is calculated as [28]:

$$(3.26) \quad D_h = \frac{2ab}{a+b}$$

Due to the small size and slow fluid flow in most of the microfluidic systems, the Reynolds number is very small, and the fluid shows a laminar behavior in the micro scale channels. However, Reynolds number is high enough to lead to turbulent flow behavior as a result of the high velocity of the fluid inside the system. Reynolds number in these experiments is calculated at the beginning of the microchannel, where the velocity is at its maximum value. A Reynolds number of above 4000 shows a turbulent flow behavior in fluidic systems [28].

3.3.4 Results and discussion

3.3.4.1 Water and PBS flow pattern analysis

Keeping all the abovementioned parameters in mind, the first microfluidic device (with a 100 μm wide microchannel and lateral wall roughness elements of 1 μm size covering the whole microchannel area) was tested with water to detect the flow patterns. The inlet pressure was gradually increased, and the fluid flow patterns were monitored with the high-speed camera in intervals of 350 kPa. The inception of cavitating flows occurred first in the extension and then in the microchannel area. The inception at the extension was visible at 3.10 MPa for the case of water.

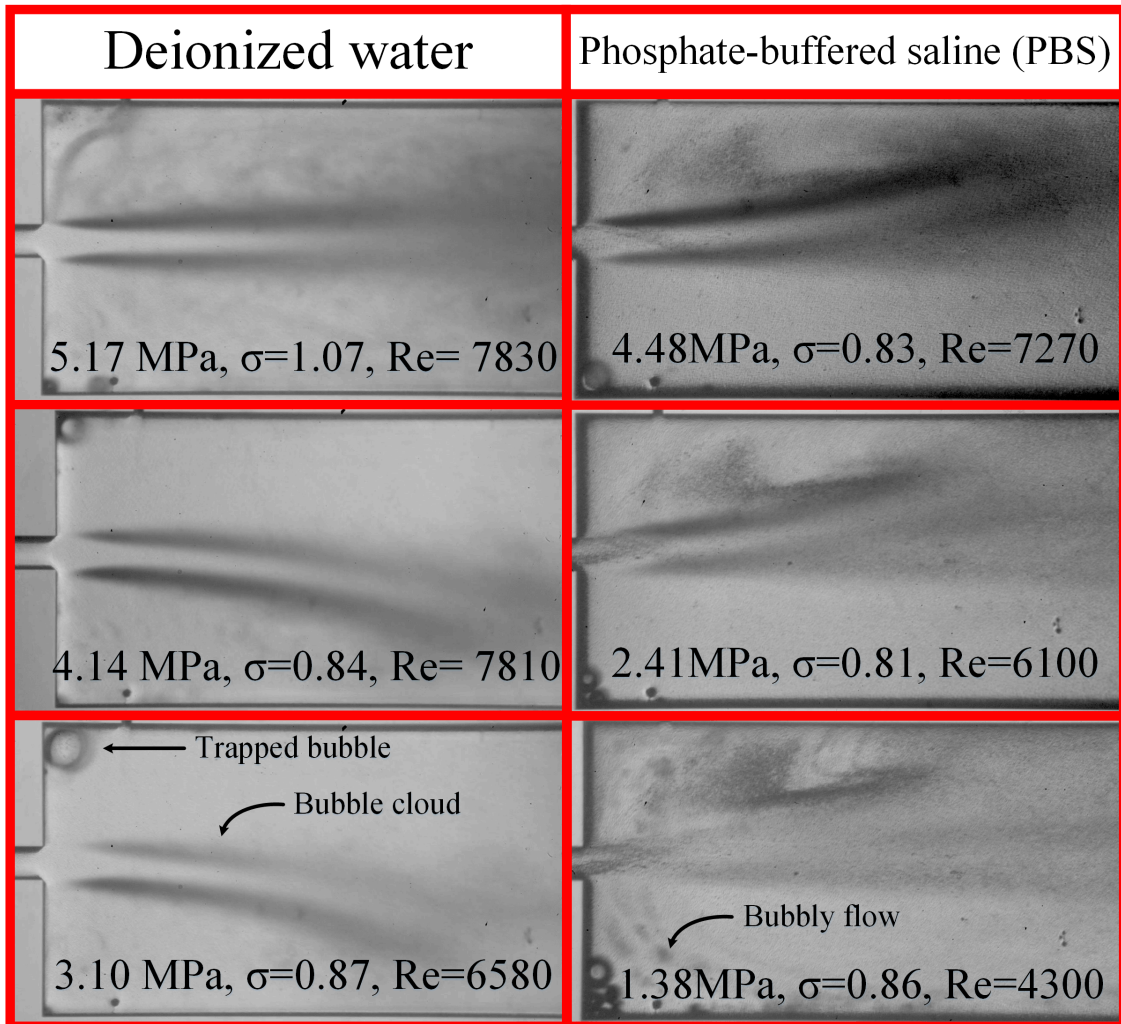
Commercial phosphate-buffered saline (PBS) (Pan Biotech Co.) was used as the working fluid in the same microfluidic device to reveal the effect of thermophysical properties of the working fluid. The inception of cavitating flows happened at a lower inlet pressure (2.41 MPa) compared with the case of water. Table (3.5) includes the thermophysical properties of water and PBS.

Table 3.5 Thermophysical properties of DI water and PBS.

	DI Water	PBS
Density (ρ) [kg/m^3]	998.2	1060
Surface tension (γ) [mN/m]	72.2	69.5
Saturation vapor pressure (P_{vap})[kPa]	2.33	2.27
Dynamic viscosity (μ) [$Pa.s$]	8.9×10^{-4}	9.04×10^{-4}

From the tensile strength point of view, PBS has a smaller surface tension compared to water. As a result, the tensile strength of the working fluid is lower than the case of water, according to Eq. (3.24). The density of PBS on the other hand is lower than water at 25 °C, which leads to a lower cavitation flowrate according to Eq. (3.23). The positive effects of both density and surface tension result in a lower inception pressure for cavitating flows. Figure (3.10) shows the flow patterns and cavitation numbers of the first microfluidic device for the cases of water and PBS.

Figure 3.10 Cavitation number and flow patterns of the first microfluidic device for the case of water and PBS.

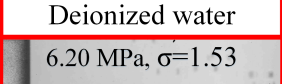
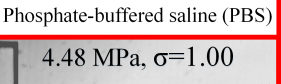
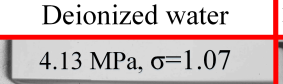
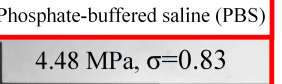
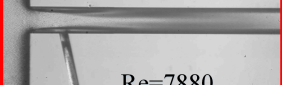
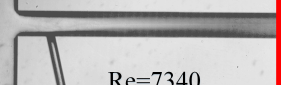
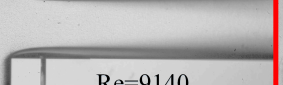
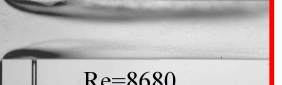
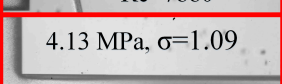
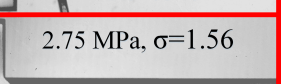
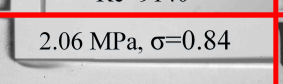
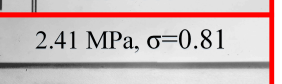


As shown in Figure Figure (3.10), PBS tends to generate bubbly flow (consists of larger bubbles with lower intensity) rather than a bubble cloud (consisting of smaller bubbles with higher intensity). The lower surface tension of PBS is the reason for this difference at low pressures [29]. In addition, the inception of cavitating flow in the nozzle is not obtained at any pressure for PBS although it happens at 3.10 MPa for the case of water (not shown in Figure (3.10)). On the other hand, the intensity of cavitating flows for PBS is more than the case of water at the same inlet pressure. This can be clearly recognized from the more intense dark lines in the extension for the case of PBS as seen in Figure (3.10). It should be noted that since the flow velocity in the microfluidic device is high, the oscillation of the twin cavities is inevitable in the extension, which is the reason for the curved gas phase in the extension. In addition, due to the high velocity of the fluid in the microchannels, the Reynolds numbers are high enough for the fluid to exhibit fully turbulent behavior. The increase in inlet pressure leads to an increase in

flow velocity. According to Eq. (3.22), cavitation number decreases under this condition. However, when the microfluidic device has the choked flow condition, the velocity does not increase with inlet pressure. As a result, the cavitation number increases beyond this point. This trend can be seen in Figure (3.10) for both working fluids. The lowest recorded cavitation number for this device corresponds to the supercavitation flow pattern. The increasing trend beyond this value implies the choked flow regime in this microfluidic device. As mentioned before, the cavitation number is an indicator for the intensity of the cavitating flow. It could be observed that the same intensity of the cavitating flow is obtained at a lower inlet pressure for the case of PBS. Almost the same cavitation number of 0.86 is obtained for both cases at pressures of 1.38 MPa and 3.10 MPa for the cases of PBS and water, respectively. The same behavior can be observed for developed flows at higher pressures, where the pressures corresponding to the same intensity of cavitating flows (cavitation number of about 0.8) are 4.14 MPa and 2.41 MPa for the cases of water and PBS, respectively.

In order to characterize the microfluidic devices (with both water and PBS) and choose the best device for the next step (deactivation of bacteria), the other two microfluidic devices with a microchannel width of 152 μm and 400 μm were tested. Figure (3.11) shows the flow patterns for the second and third devices for the cases of water and PBS.

Figure 3.11 Reynolds and cavitation numbers and flow patterns of the second and third microfluidic device for the cases of water and PBS.

The second device		The third device	
Deionized water	Phosphate-buffered saline (PBS)	Deionized water	Phosphate-buffered saline (PBS)
6.20 MPa, $\sigma=1.53$  Re=7880	4.48 MPa, $\sigma=1.00$  Re=7340	4.13 MPa, $\sigma=1.07$  Re=9140	4.48 MPa, $\sigma=0.83$  Re=8680
4.13 MPa, $\sigma=1.09$  Re=7630	2.75 MPa, $\sigma=1.56$  Re=5060	2.06 MPa, $\sigma=0.84$  Re=7680	2.41 MPa, $\sigma=0.81$  Re=6570
3.10 MPa, $\sigma=1.65$  Re=5550	1.86 MPa, $\sigma=2.44$  Re=4640	1.79 MPa, $\sigma=0.87$  Re=5480	1.24 MPa, $\sigma=0.86$  Re=3590

As expected and explained in Section (3.3.3), the velocity of the fluid flow is high enough to have fully turbulent behavior in the microchannel. The Reynolds numbers in Figure (3.11) are all above 4000. The cavitation number was also been calculated

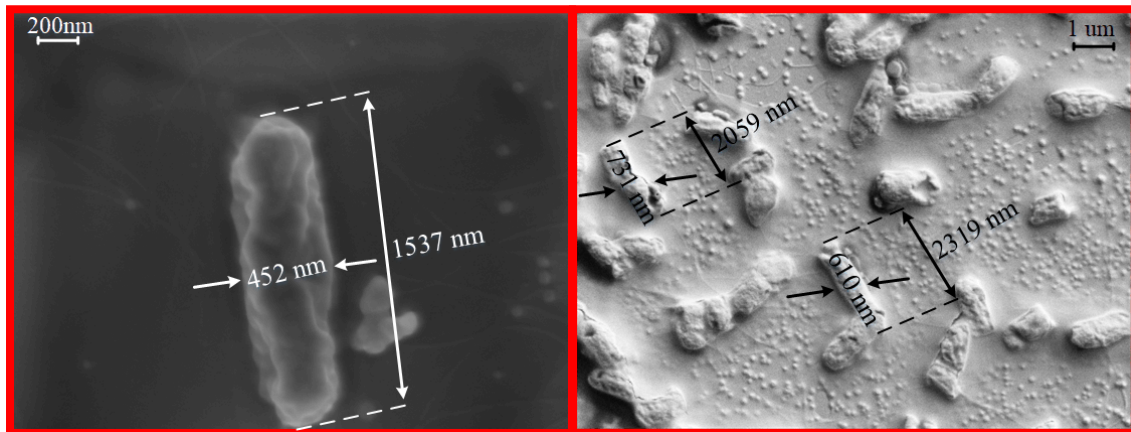
for the second and third devices at different inlet pressures. The results show that the intensity of cavitating flow for the case of PBS is more than the intensity for the case of water, which can be concluded from the experimental results of the second device at the highest inlet pressure. As can be seen, the Reynolds numbers are almost the same, while the cavitation numbers are different, which is due to the difference between the thermophysical properties of the working fluids. Likewise, in the third device, the flow shows fully turbulent behavior based on the calculated Reynolds numbers. As shown in Figure (3.11), the cavitation numbers in this device are lower than those in the second device, which implies more intense cavitating flows in the microchannel. As a result, the third device is a more suitable candidate for bacteria deactivation. Thus, this microfluidic device is considered in the following section.

3.3.4.2 Bacteria/PBS suspension flow pattern analysis

The nucleation of cavitating bubbles in a fluidic system could be categorized as homogeneous and heterogeneous nucleation. In homogeneous nucleation, bubbles form in the bulk of fluid at the nucleation sites. From a microscopic point of view, the molecules with high kinetic energy as a result of high energy physical collisions with other molecules are susceptible in a fluid to phase change at low pressure regions. On the other hand, surface tension, as discussed in Section (3.3.3), plays a crucial role in homogeneous nucleation. Heterogeneous nucleation, on the other hand, occurs on the interface of solid and liquid phases, such as in the vicinity of the walls in the microfluidic device. This kind of nucleation could also originate from sub-micron size contaminations such as solid particles in the working fluid. The inevitable presence of external particles in fluidic systems (even after using filters) has made homogeneous nucleation studies challenging for the researchers.

In this part of the experiments, the suspended *S. typhimurium* in PBS acts as the external solid particles in the fluid and forms the interface of liquid and solid to enhance the intensity of cavitating flows. The irregular shape of the bacteria with a porous surface intensifies cavitating flows in the microfluidic devices. Figure (3.12) shows the SEM images of the bacteria before the experiments. The nominal length of *S. typhimurium* bacteria is ranging from 1000 to 2500 nm according to SEM images. As can be seen in this figure, they are rod-shaped. It is worth mentioning that flagella around bacteria are obvious and noticeable in the 200 nm-scale images of Figure (3.12).

Figure 3.12 SEM imaged of the bacteria before the experiments.



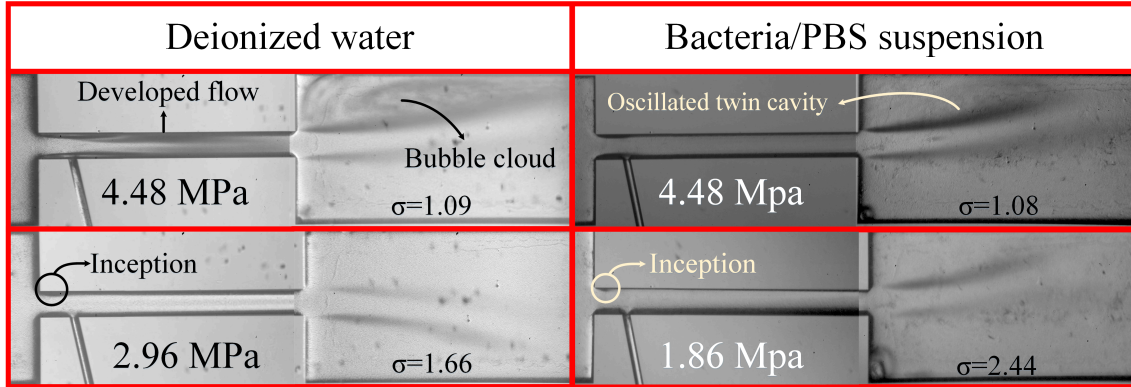
Since the width of the microfluidic device used in the previous section is small, the bacteria would agglomerate at the nozzle entrance and block the microfluidic device. The high-pressure fluid could also lead to the explosion of the device. To overcome this problem, the width of the microfluidic device is first raised to 152 μm and then to 400 μm in the following section. On the other hand, based on our previous study, the shorter total length of the lateral roughness elements leads to lower energy requirement to obtain high intensity cavitating flows. As a result, the lateral roughness elements cover one third of the microchannel length in the proposed microfluidic devices.

In order to run the experiments with bacteria, the fluidic system had to be cleaned and sterilized. For this purpose, 100 % bleach was passed through the system for several times for 30 minutes. Then, 70 % ethanol was used to clean the fluidic system for 30 minutes by passing it through the system. At the end, autoclaved water was used to sterilize the system for 30 minutes before using the bacteria suspension. The serological pipettes were used to load the sample to the fluid container before the tests. After loading the bacteria suspension, the inlet pressure was gradually increased to monitor the flow behavior with the high speed camera. The inception of cavitating flow is recorded at 1.86 MPa for the second microfluidic device, while the same flow pattern is obtained at 2.96 MPa for the case of water.

The inception of cavitation flow and the cavity movement along the microchannel area for the case of water are more intense than the bacteria suspension case. This is due to tensile strength change due to the presence of bacteria in the working fluid. Another difference between the flow patterns lies in the development of the cavitating flow in the microchannel area. The developed cavitating flow happens at 4.48 MPa for the case of water, whereas it never happens for the case of bacteria. This is despite the fact that the intensity of cavitating flow in the extension is more

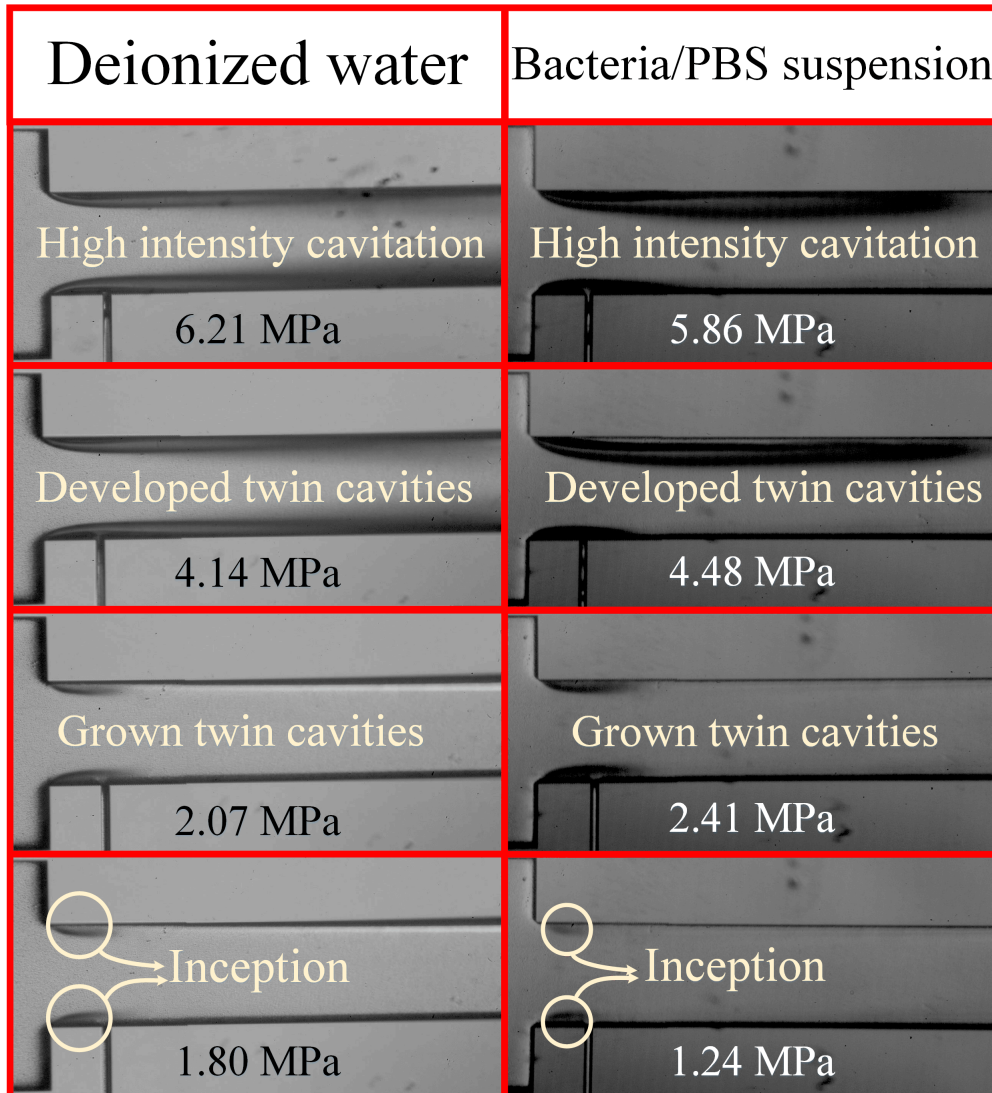
for the case of bacteria but not in the microchannel. Figure (3.13) compares the flow patterns of the second device for the cases of water and bacteria suspension.

Figure 3.13 The flow pattern of the second device working with water and bacteria suspension (merged images from high speed camera).



Because of the frequent clogging of the device with bacteria especially at the entrance of the microchannel area, the third device with the mentioned geometrical dimensions was tested with the same bacteria suspension. The inception of cavitating flows is recorded at 1.03 MPa in the microchannel area for this device, while the inception pressure for the case of water is 2.06 MPa. Figure (3.14) shows the flow patterns of the cases of water and bacteria suspension along the channel. As can be seen, the intensity of cavitating flows is more in the case of bacteria suspension compared to water. Due to safety considerations, the tests with bacteria suspension are not performed at pressures higher than 5.65 MPa. The cavitation number, as explained via Eq. (3.22), depends on the inlet pressure, saturation vapor pressure, velocity, and density of the working fluid. As a result, increasing the inlet pressure leads to a decrease in the cavitation number. Under the choked flow condition, where the flowrate in the microfluidic device is saturated, the velocity does not increase with the inlet pressure. As a result, the cavitation number increases beyond this point.

Figure 3.14 The fluid flow pattern of water and bacteria suspension in the third microfluidic device.



3.3.4.3 Bacteria deactivation of hydrodynamic cavitation

The cavitation bubbles carry a potential energy relative to the size of the bubbles as demonstrated in Eq. (3.27) [30]:

$$(3.27) \quad E_{pot} = \frac{4}{3}\pi R^3(P_{sat} - P_{vap})$$

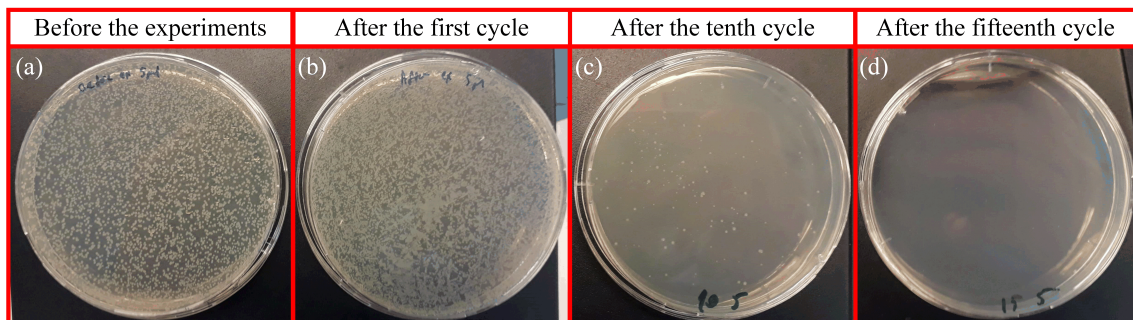
where R is the radius of the generated bubbles, and P is the static pressure of the

working fluid. The carrying potential energy by each bubble is converted to heat, vibration, noise, and shock wave upon collapse, thereby generating high pressure and temperature local points. The released energy by the bubbles affects the viability of the bacteria suspended in the working fluid. In order to study this effect, the exiting fluid from the microfluidic device was collected in a sterile container and was reloaded to the fluid container by sterile serological pipettes for several times, and the viability study was performed after the first, tenth, and fifteenth cycles.

In order to determine the antibacterial activity of the cavitation processes, bacteria suspensions collected before and after the cavitation flow assays were plated on the LB agar medium at 1:10 dilution and incubated overnight in order to check for the bacterial growth on the cavitated and the control samples.

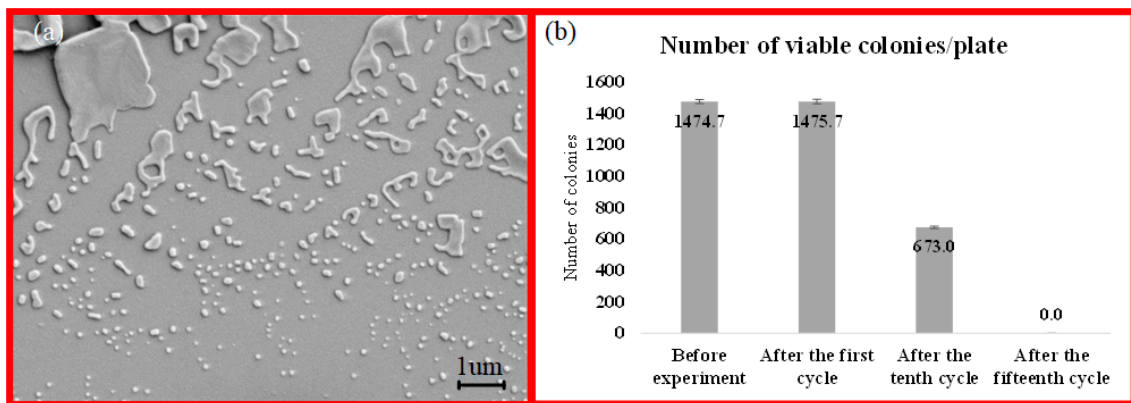
The clogging problem happened for the second device as well. As a result, the deactivation effect of cavitating flow was only investigated in the third device under the developed flow condition obtained at the inlet pressure of 4.48 MPa. Figure (3.15-a) shows the complete growth of bacteria on the control agar plate before the experiment and also after the first cycle of cavitating flow in the microfluidic device (Figure (3.15-b)). The bacteria seem intact as a result of the cavitating flow after the first cycle, and the number of colonies does not change considerably. This is due to the short exposure of bacteria to collapsing bubbles after the first cycle. However, Figure (3.15-c) demonstrates a significant decrease in the number of bacteria colonies after the tenth cycle, while Figure (3.15-d) demonstrates complete deactivation of the bacteria after the fifteenth cycle. Each cycle of the cavitating flow took less than 3 minutes for 250 ml of the bacteria suspension. A bacteria deactivation efficiency of 100 % can be attained with this device within 45 minutes of the system operation.

Figure 3.15 Bacteria colonies on the agar plates exposed to developed cavitating flow at inlet pressure of 4.48 MPa, a) complete growth of the bacteria before the experiments, b) no significant change in the number of colonies after the first cycle of the cavitation (approximately 3 minutes), c) a significant decrease in the number of active colonies after the tenth cycle of the hydrodynamic cavitation (approximately 30 minutes), d) complete deactivation of the bacteria after the fifteenth cycle of the experiments (approximately 45 minutes).



SEM analysis of the sample after the cavitation assay (Figure (3.16-a), which was prepared on a silicon substrate using the same methodology as explained in Section 3.3.3, agrees with Figure (3.15-d), where no bacteria colony is visible on the agar plate after 15 cycles. Figure (3.16-b) displays bacteria colony numbers, which were determined by using the digital image analysis software ImageJ [31]. The data was presented as the mean of three software-based bacterial colony measurements. As can be seen, the colony number decreases with the number of cycles, which suggests the effectiveness of the ‘Cavitation on Chip’ concept in deactivation.

Figure 3.16 a) SEM analysis of the sample after the cavitation assay, b) the quantitative data of the bacteria colony number.



3.3.4.4 Conclusions

In the first part of this study, water and PBS were tested as the working fluids in the fabricated microfluidic devices, and the differences in the flow behavior was discussed with the perspective of thermophysical differences. The results confirmed the importance of surface tension and density of the working fluid for the nucleation of cavitating bubbles. The inception of hydrodynamic cavitation at the inlet happened at 2.41 MPa for the case of PBS, while it occurred at 3.10 MPa for the case of water. The tendency of PBS to form bubbly flow rather than bubble cloud was also recognized. The intensity of cavitating flows in the extension of the microfluidic devices was also another difference between the working fluids in this study. PBS lead to a more intense cavitation flow regime in the extension compared to the case of water.

The second part of this study is dedicated to the effect of the presence of *S. typhimurium* in the working fluid on the flow patterns. The irregular shape of the bacteria in the working fluid acted as a solid interface, which promoted the inception

of cavitation by increasing the heterogeneous nucleation sites. The energy release upon collapse of the cavitating bubbles had an impact on the viability of the bacteria in the working fluid. The viability test on the suspended bacteria in the fluid exhibited a significant decrease in the colony number of bacteria after experiments. A deactivation efficiency of 100 % was attained in the designed microfluidic devices. A change in the design of the microfluidic devices, such as putting more micro-orifices on one chip, could further augment the output of the system. On the other hand, in some applications such as energy harvesting, intensifying the cavitating flow in microfluidic devices is of great importance. Reaching developed cavitating flows at lower inlet pressures could increase the efficiency of energy harvesting systems. Hence, using bacteria (non-toxic species) in the working fluid with this purpose could be a solution to raise the efficiency of energy harvesting systems, which are based on the 'Hydrodynamic Cavitation on Chip' concept. The major advantages of the proposed system are the low cost of fabrication and high bacteria deactivation efficiency.

The proposed concept in the study could be well utilized for energy harvesting as well as for water treatment. Since bacteria are found abundant in the nature, and their culturing is not a very costly procedure, they could be considered as strong candidates in energy harvesting systems to enhance the performance. The species of the bacteria could be changed in this regard to ensure a safe and more environmentally friendly platform. In addition, the design of such microfluidic devices could be further optimized.

4. Chapter four: Conclusion

This thesis is dedicated to the physics and applications of hydrodynamic cavitation in high resistive microfluidic devices. Hydrodynamic cavitation is a significant phase change phenomenon, which occurs as a result of static pressure drop beyond a critical value. The required pressure drop in the present systems is obtained by sudden drop in cross sectional area of the fluid flow path. Hydrodynamic cavitation process consists of inception of cavitating flow, development of cavities, and bubbles explosion. The generated micro-sized bubbles release a huge amount of energy at their collapse which is used for different applications.

In this regard, facile hydrodynamic cavitation was characterized to reach the highest achievable energy upon the collapse of cavitation bubbles. Different parameters such as geometry of the microfluidic device, thermophysical properties of the working fluid, and roughness elements play a crucial role in this subject. The mentioned influential parameters are the main concern of this thesis.

In order to study the physics of hydrodynamic cavitation, 11 microfluidic devices with different geometrical designs were fabricated according to the techniques adopted from semiconductor based micro- fabrication. An experimental setup was designed and assembled to acquire high pressure hydrodynamic cavitation and characterize the fluid flow pattern.

In the first set of experiments, 7 microfluidic devices were chosen and tested at different inlet pressures. The effect of lateral wall roughness elements was the focus of this study. The results revealed the optimum design area for hydrodynamic cavitation in the fabricated devices. This study continued with the effect of ethanol on the flow pattern. The results showed that hydrodynamic cavitation is sensitive to surface tension effects as well as saturation vapor pressure of the working fluid.

The second and third sets of experiments were mainly concerned with the applications of hydrodynamic cavitation. First the capability of these devices in energy harvesting was studied. For this purpose, three microfluidic devices were chosen and tested on the experimental setup. The performances of the devices were eval-

uated analytically. In this regard, a control volume was assumed at the beginning of the nozzle section of the microfluidic devices and the number of the bubbles were calculated in that. Assuming a supercavitation condition, the potential energy of the bubbles were calculated and the heat energy upon collapse was analytically discussed. On the other hand, two μ -TEGs were placed at the end of the devices so that the heat energy could heat on side of them. The energy generation of the devices in this working condition was calculated over time. In another set of experiments, the working fluid was replaced with the suspension of PFC5 droplets in water. Because of the difference in thermophysical properties of the working fluids, the performance of the devices was enhanced and more intense cavitating flow was obtained at lower inlet pressures. This way, the working efficiency of the microfluidic devices could be modified.

The last sets of experiments were on the bacteria deactivation capability of the hydrodynamic cavitation. The presence of high pressure and high temperature local points at the bubble collapse along with the high intensity micro jets were proven to be effective in removing bacteria from the working fluid. For this purpose, *Salmonella typhimurium* bacteria was suspended in PBS and used as the working fluid. The experiments were done over and over again and samples were collected at different steps. The results showed a complete removal and deactivation of the bacteria after 15 cycles of hydrodynamic cavitation treatment. As compared to the present water treatment reactors available in the literature, the fabricated microfluidic devices showed a very high removal efficiency. Besides this, the presence of bacteria in the working fluid enriched the heterogeneous nucleation points and helped to obtain cavitating flow in lower inlet pressures. In addition, pure PBS was used as the working fluid in the devices as well and the performance of the fluidic system was compared with the case of water. The results were in line with ethanol and PFC5 droplets suspension usage.

As a conclusion, the presented microfluidic devices in this thesis accommodate a unique geometry as compared to the available devices in the literature. The advantages of these devices are the high pressure resistance capability, high intensity cavitating flow, and the presence of local vortices in the extension area. These devices are cheap and easy to fabricate and since they have no moving part, the operation is also easy to handle and implement in different applications.

4.1 Future Research Directions

This thesis presents a high efficiency hydrodynamic cavitation reactor, which could be used in energy harvesting and bacteria disinfection. However, the working efficiency of the system could be enhanced by altering the design of either the microfluidic devices or the experimental setup. For this purpose, one can come up with a new design that facilitates the parallel working possibility for multiple devices. The parallel working condition could increase the out flow of the system for energy harvesting and bacteria deactivation applications.

Implementing surface roughness elements in the microfluidic devices could also help in increasing the efficiency and intensity of the hydrodynamic cavitation.

In addition, the present hydrodynamic system could be used in other applications such as cancer diagnosis and therapy or removal of other pollutions such as viruses and industrial pollutions from water and wastewater sources.

Finally, since flow patterns are characterized in this thesis and repetitive trends are observed at different inlet pressures, the devices could be used for pressure or temperature sensor design and fabrication. Correlating the inlet pressure with the flow pattern could be beneficial for this purpose.

BIBLIOGRAPHY

- [1] Osborne Reynolds. The causes of the racing of the engines of screw steamers investigated theoretically and by experiment. *Trans. Inst. Naval Arch*, 14:56–67, 1873.
- [2] Charles Parsons. *The Steam Turbine on Land at Sea*. Smithsonian Inst., 1908.
- [3] Roger EA Arndt. Cavitation in fluid machinery and hydraulic structures. *Annual Review of Fluid Mechanics*, 13(1):273–326, 1981.
- [4] Christopher E Brennen. *Cavitation and bubble dynamics*. Cambridge University Press, 2014.
- [5] Song-Sheng Deng, Guo-Dong Li, Jin-Fa Guan, Xiao-Chen Chen, and Lu-Xing Liu. Numerical study of cavitation in centrifugal pump conveying different liquid materials. *Results in Physics*, 12:1834–1839, 2019.
- [6] Xavier Escaler, Eduard Egusquiza, Mohamed Farhat, Francois Avellan, and Miguel Coussirat. Detection of cavitation in hydraulic turbines. *Mechanical systems and signal processing*, 20(4):983–1007, 2006.
- [7] Morteza Ghorbani, Ali Mohammadi, Ahmad Reza Motezakker, Luis Guillermo Villanueva, Yusuf Leblebici, and Ali Kosar. Energy harvesting in microscale with cavitating flows. *ACS omega*, 2(10):6870–6877, 2017.
- [8] Andrej Šarc, Tadej Stepišnik-Perdih, Martin Petkovšek, and Matevž Dular. The issue of cavitation number value in studies of water treatment by hydrodynamic cavitation. *Ultrasonics sonochemistry*, 34:51–59, 2017.
- [9] Matevž Dular, Tjaša Griessler-Bulc, Ion Gutierrez-Aguirre, Ester Heath, Tina Kosjek, Aleksandra Krivograd Klemenčič, Martina Oder, Martin Petkovšek, Nejc Rački, Maja Ravnikar, et al. Use of hydrodynamic cavitation in (waste) water treatment. *Ultrasonics sonochemistry*, 29:577–588, 2016.
- [10] Morteza Ghorbani, Canberk Sozer, Gokhan Alcan, Mustafa Unel, Sinan Ekici, Huseyin Uvet, and Ali Koşar. Biomedical device prototype based on small scale hydrodynamic cavitation. *AIP Advances*, 8(3):035108, 2018.
- [11] Lorenzo Albanese, Rosaria Ciriminna, Francesco Meneguzzo, and Mario Pagliaro. Beer-brewing powered by controlled hydrodynamic cavitation: Theory and real-scale experiments. *Journal of Cleaner Production*, 142:1457–1470, 2017.
- [12] Mehrdad Karimzadehkhoei, Morteza Ghorbani, Meltem Sezen, Kürşat Şendur, M Pınar Mengüç, Yusuf Leblebici, and Ali Koşar. Increasing the stability of nanofluids with cavitating flows in micro orifices. *Applied Physics Letters*, 109(10):104101, 2016.

- [13] Moein Talebian Gevari, Taher Abbasiasl, Soroush Niazi, Morteza Ghorbani, and Ali Kosar. Direct and indirect thermal applications of hydrodynamic and acoustic cavitation: A review. *Applied Thermal Engineering*, page 115065, 2020.
- [14] Richard Edwin Sonntag, Claus Borgnakke, Gordon John Van Wylen, and Steve Van Wyk. *Fundamentals of thermodynamics*, volume 6. Wiley New York, 1998.
- [15] David J Flannigan and Kenneth S Suslick. Plasma formation and temperature measurement during single-bubble cavitation. *Nature*, 434(7029):52–55, 2005.
- [16] Mandar Badve, Parag Gogate, Aniruddha Pandit, and Levente Csoka. Hydrodynamic cavitation as a novel approach for wastewater treatment in wood finishing industry. *Separation and purification technology*, 106:15–21, 2013.
- [17] Mojca Zupanc, Tina Kosjek, Martin Petkovšek, Matevž Dular, Boris Kompare, Brane Širok, Marjeta Stražar, and Ester Heath. Shear-induced hydrodynamic cavitation as a tool for pharmaceutical micropollutants removal from urban wastewater. *Ultrasonics sonochemistry*, 21(3):1213–1221, 2014.
- [18] Daolun Feng, Jie Zhao, and Tian Liu. Inactivation of heterosigma akashiwo in ballast water by circular orifice plate-generated hydrodynamic cavitation. *Environmental technology*, 37(7):837–846, 2016.
- [19] Ruly Terán Hilares, Lucas Ramos, Silvio Silvério da Silva, Giuliano Dragone, Solange I Mussatto, and Júlio César dos Santos. Hydrodynamic cavitation as a strategy to enhance the efficiency of lignocellulosic biomass pretreatment. *Critical reviews in biotechnology*, 38(4):483–493, 2018.
- [20] Parag R Gogate, Irfan Z Shirgaonkar, M Sivakumar, P Senthilkumar, Nilesh P Vichare, and Aniruddha B Pandit. Cavitation reactors: efficiency assessment using a model reaction. *AIChE journal*, 47(11):2526–2538, 2001.
- [21] Parag R Gogate and Aniruddha B Pandit. A review and assessment of hydrodynamic cavitation as a technology for the future. *Ultrasonics sonochemistry*, 12(1-2):21–27, 2005.
- [22] Chandan Mishra and Yoav Peles. Cavitation in flow through a micro-orifice inside a silicon microchannel. *Physics of fluids*, 17(1):013601, 2005.
- [23] Matevž Dular, I Khlifa, Sylvie Fuzier, M Adama Maiga, and Olivier Coutier-Delgosha. Scale effect on unsteady cloud cavitation. *Experiments in fluids*, 53(5):1233–1250, 2012.
- [24] Chandan Mishra and Yoav Peles. An experimental investigation of hydrodynamic cavitation in micro-venturis. *Physics of Fluids*, 18(10):103603, 2006.
- [25] J Li and P Cheng. Bubble cavitation in a microchannel. *International journal of heat and mass transfer*, 47(12-13):2689–2698, 2004.

- [26] M Medrano, PJ Zermatten, Christian Pellone, Jean-Pierre Franc, and Frédéric Ayela. Hydrodynamic cavitation in microsystems. i. experiments with deionized water and nanofluids. *Physics of Fluids*, 23(12):127103, 2011.
- [27] Chandan Mishra and Yoav Peles. Size scale effects on cavitating flows through microorifices entrenched in rectangular microchannels. *Journal of microelectromechanical systems*, 14(5):987–999, 2005.
- [28] D Podbevsek, Damien Colombet, Gilles Ledoux, and Frédéric Ayela. Observation of chemiluminescence induced by hydrodynamic cavitation in microchannels. *Ultrasonics sonochemistry*, 43:175–183, 2018.
- [29] Frédéric Ayela, Manuel Medrano-Munoz, David Amans, Christophe Dujardin, Thomas Brichart, Matteo Martini, Olivier Tillement, and Gilles Ledoux. Experimental evidence of temperature gradients in cavitating microflows seeded with thermosensitive nanoprobles. *Physical Review E*, 88(4):043016, 2013.
- [30] M Medrano, Christian Pellone, PJ Zermatten, and Frédéric Ayela. Hydrodynamic cavitation in microsystems. ii. simulations and optical observations. *Physics of Fluids*, 24(4):047101, 2012.
- [31] Stéphane Mossaz, Damien Colombet, and Frédéric Ayela. Hydrodynamic cavitation of binary liquid mixtures in laminar and turbulent flow regimes. *Experimental Thermal and Fluid Science*, 80:337–347, 2017.
- [32] Zhixia He, Wenjun Zhong, Qian Wang, Zhaochen Jiang, and Zhuang Shao. Effect of nozzle geometrical and dynamic factors on cavitating and turbulent flow in a diesel multi-hole injector nozzle. *International Journal of Thermal Sciences*, 70:132–143, 2013.
- [33] Pavel Rudolf, Dávid Kubina, Martin Hudec, Jiří Kozák, Blahoslav Maršálek, Eliška Maršálková, and František Pochylý. Experimental investigation of hydrodynamic cavitation through orifices of different geometries. In *EPJ Web of Conferences*, volume 143, page 02098. EDP Sciences, 2017.
- [34] Zhi Yong Dong, Qi Qi Chen, Yong Gang Yang, and Bin Shi. Experimental and numerical study of hydrodynamic cavitation of orifice plates with multiple triangular holes. In *Applied Mechanics and Materials*, volume 256, pages 2519–2522. Trans Tech Publ, 2013.
- [35] Alister Simpson and Vivek V Ranade. Modelling of hydrodynamic cavitation with orifice: Influence of different orifice designs. *Chemical Engineering Research and Design*, 136:698–711, 2018.
- [36] Zhi-jiang Jin, Zhi-xin Gao, Xiao-juan Li, and Jin-yuan Qian. Cavitating flow through a micro-orifice. *Micromachines*, 10(3):191, 2019.
- [37] Morteza Ghorbani, Gökberk Deprem, Ece Ozdemir, Ahmad Reza Motezakker, L Guillermo Villanueva, and Ali Koşar. On “cavitation on chip” in microfluidic devices with surface and sidewall roughness elements. *Journal of Microelectromechanical Systems*, 28(5):890–899, 2019.

- [38] Kyoung-Su Im, Seong-Kyun Cheong, Christopher F Powell, D Lai Ming-chia, and Jin Wang. Unraveling the geometry dependence of in-nozzle cavitation in high-pressure injectors. *Scientific reports*, 3:2067, 2013.
- [39] Jitendra Carpenter, Suja George, and Virendra Kumar Saharan. Low pressure hydrodynamic cavitating device for producing highly stable oil in water emulsion: Effect of geometry and cavitation number. *Chemical Engineering and Processing: Process Intensification*, 116:97–104, 2017.
- [40] Morteza Ghorbani, Abdolali K Sadaghiani, L Guillermo Villanueva, and Ali Koşar. Hydrodynamic cavitation in microfluidic devices with roughened surfaces. *Journal of Micromechanics and Microengineering*, 28(7):075016, 2018.
- [41] Morteza Ghorbani, Araz Sheibani Aghdam, Moein Talebian Gevari, Ali Koşar, Fevzi Çakmak Cebeci, Dmitry Grishenkov, and Anna J Svagan. Facile hydrodynamic cavitation on chip via cellulose nanofibers stabilized perfluorodroplets inside layer-by-layer assembled slips surfaces. *Chemical Engineering Journal*, 382:122809, 2020.
- [42] Moein Talebian Gevari, Ali Hosseinpour Shafaghi, Luis Guillermo Villanueva, Morteza Ghorbani, and Ali Koşar. Engineered lateral roughness element implementation and working fluid alteration to intensify hydrodynamic cavitating flows on a chip for energy harvesting. *Micromachines*, 11(1):49, 2020.
- [43] Randip Singh and Yoav Peles. The effects of fluid properties on cavitation in a micro domain. *Journal of Micromechanics and Microengineering*, 19(2):025009, 2009.
- [44] Chandan Mishra and Yoav Peles. Development of cavitation in refrigerant (r-123) flow inside rudimentary microfluidic systems. *Journal of microelectromechanical systems*, 15(5):1319–1329, 2006.
- [45] Morteza Ghorbani, Hongjian Chen, Luis Guillermo Villanueva, Dmitry Grishenkov, and Ali Koşar. Intensifying cavitating flows in microfluidic devices with poly (vinyl alcohol)(pva) microbubbles. *Physics of Fluids*, 30(10):102001, 2018.
- [46] Taher Abbasasl, Soroush Niazi, Araz Sheibani Aghdam, Hongjian Chen, Fevzi Çakmak Cebeci, Morteza Ghorbani, Dmitry Grishenkov, and Ali Koşar. Effect of intensified cavitation using poly (vinyl alcohol) microbubbles on spray atomization characteristics in microscale. *AIP Advances*, 10(2):025318, 2020.
- [47] Wei Li, Yongfei Yang, Wei-dong Shi, Xiaofan Zhao, and Weiqiang Li. The correction and evaluation of cavitation model considering the thermodynamic effect. *Mathematical Problems in Engineering*, 2018, 2018.
- [48] Side Cases. Annual energy outlook 2019 release date: January 24, 2019| next release date: January 2020| full report.
- [49] Kenneth S Suslick, Nathan C Eddingsaas, David J Flannigan, Stephen D Hopkins, and Hangxun Xu. Extreme conditions during multibubble cavitation: Sonoluminescence as a spectroscopic probe. *Ultrasonics sonochemistry*, 18(4):842–846, 2011.

- [50] Wenhua Zhang, Juekuan Yang, and Dongyan Xu. A high power density microthermoelectric generator fabricated by an integrated bottom-up approach. *Journal of Microelectromechanical Systems*, 25(4):744–749, 2016.
- [51] Reinhard Roth, Raimar Rostek, Keith Cobry, Christian Köhler, Moritz Groh, and Peter Woias. Design and characterization of micro thermoelectric cross-plane generators with electroplated Bi_2Te_3, Sb_xTe_y , and reflow soldering. *Journal of microelectromechanical systems*, 23(4):961–971, 2014.
- [52] Wendong Shi, Lei Wang, and Baiyang Chen. Kinetics, mechanisms, and influencing factors on the treatment of haloacetonitriles (hans) in water by two household heating devices. *Chemosphere*, 172:278–285, 2017.
- [53] Oscar Casas-Monroy, Robert D Linley, Po-Shun Chan, Jocelyn Kydd, Julie Vanden Byllaardt, and Sarah Bailey. Evaluating efficacy of filtration+uv-c radiation for ballast water treatment at different temperatures. *Journal of Sea Research*, 133:20–28, 2018.
- [54] Nannan Wang and Peng Wang. Study and application status of microwave in organic wastewater treatment—a review. *Chemical Engineering Journal*, 283:193–214, 2016.
- [55] Arun Subramani and Joseph G Jacangelo. Emerging desalination technologies for water treatment: a critical review. *Water research*, 75:164–187, 2015.
- [56] CAO Yang, QU Guangzhou, LI Tengfei, Nan Jiang, and WANG Tiecheng. Review on reactive species in water treatment using electrical discharge plasma: formation, measurement, mechanisms and mass transfer. *Plasma Science and Technology*, 20(10):103001, 2018.
- [57] Adel Al-Kdasi, Azni Idris, Katayon Saed, and Chuah Teong Guan. Treatment of textile wastewater by advanced oxidation processes—a review. *Global nest: the Int. J.*, 6(3):222–230, 2004.
- [58] Kian Mun Lee, Chin Wei Lai, Koh Sing Ngai, and Joon Ching Juan. Recent developments of zinc oxide based photocatalyst in water treatment technology: a review. *Water research*, 88:428–448, 2016.
- [59] Alexander Kraft. Electrochemical water disinfection: a short review. *Platinum metals review*, 52(3):177–185, 2008.
- [60] BR Kim, JE Anderson, SA Mueller, WA Gaines, and AM Kendall. Literature review—efficacy of various disinfectants against legionella in water systems. *Water Research*, 36(18):4433–4444, 2002.
- [61] Mark J Nieuwenhuijsen, Mireille B Toledano, Naomi E Eaton, John Fawell, and Paul Elliott. Chlorination disinfection byproducts in water and their association with adverse reproductive outcomes: a review. *Occupational and environmental medicine*, 57(2):73–85, 2000.
- [62] Krishna Gopal, Sushree Swarupa Tripathy, Jean Luc Bersillon, and Shashi Prabha Dubey. Chlorination byproducts, their toxicodynamics and

- removal from drinking water. *Journal of hazardous materials*, 140(1-2):1–6, 2007.
- [63] Xun Sun, Jong Jin Park, Hyun Soo Kim, Seung Ho Lee, Si Jin Seong, Ae Son Om, and Joon Yong Yoon. Experimental investigation of the thermal and disinfection performances of a novel hydrodynamic cavitation reactor. *Ultrasonics sonochemistry*, 49:13–23, 2018.
- [64] Woo Chul Kwon and Joon Yong Yoon. Experimental study of a cavitation heat generator. *Proceedings of the Institution of Mechanical Engineers, Part E: Journal of Process Mechanical Engineering*, 227(1):67–73, 2013.
- [65] Matevž Dular. Hydrodynamic cavitation damage in water at elevated temperatures. *Wear*, 346:78–86, 2016.
- [66] Efi Tsolaki and Evan Diamadopoulos. Technologies for ballast water treatment: a review. *Journal of Chemical Technology & Biotechnology*, 85(1):19–32, 2010.
- [67] Andrej Šarc, Martina Oder, and Matevž Dular. Can rapid pressure decrease induced by supercavitation efficiently eradicate legionella pneumophila bacteria? *Desalination and Water Treatment*, 57(5):2184–2194, 2016.
- [68] S Arrojo, Y Benito, and A Martínez Tarifa. A parametrical study of disinfection with hydrodynamic cavitation. *Ultrasonics Sonochemistry*, 15(5):903–908, 2008.
- [69] L Mezule, S Tsyfansky, V Yakushevich, and Tālis Juhna. A simple technique for water disinfection with hydrodynamic cavitation: effect on survival of escherichia coli. *Desalination*, 248(1-3):152–159, 2009.
- [70] Gregory Loraine, Georges Chahine, Chao-Tsung Hsiao, Jin-Keun Choi, and Patrick Aley. Disinfection of gram-negative and gram-positive bacteria using dynajets® hydrodynamic cavitating jets. *Ultrasonics sonochemistry*, 19(3):710–717, 2012.
- [71] Eva F Karamah, Rioneli Ghaudenson, Fitri Amalia, and Setijo Bismo. Disinfection of escherichia coli bacteria using hybrid method of ozonation and hydrodynamic cavitation with orifice plate. In *AIP Conference Proceedings*, volume 1904, page 020075. AIP Publishing LLC, 2017.
- [72] Xiaowei Su, Svetlana Zivanovic, and Doris H D’Souza. Inactivation of human enteric virus surrogates by high-intensity ultrasound. *Foodborne pathogens and disease*, 7(9):1055–1061, 2010.
- [73] Janez Kosel, Ion Gutiérrez-Aguirre, Nejc Rački, Tanja Dreo, Maja Ravnikar, and Matevž Dular. Efficient inactivation of ms-2 virus in water by hydrodynamic cavitation. *Water research*, 124:465–471, 2017.
- [74] Patrick Braeutigam, Marcus Franke, Rudolf J Schneider, Andreas Lehmann, Achim Stolle, and Bernd Ondruschka. Degradation of carbamazepine in environmentally relevant concentrations in water by hydrodynamic-acoustic-cavitation (hac). *Water research*, 46(7):2469–2477, 2012.

- [75] Martin Petkovšek, Mojca Zupanc, Matevž Dular, Tina Kosjek, Ester Heath, Boris Kompare, and Brane Širok. Rotation generator of hydrodynamic cavitation for water treatment. *Separation and purification technology*, 118:415–423, 2013.
- [76] Jun Wang, Yuefeng Jiang, Zhaohong Zhang, Xiangdong Zhang, Teng Ma, Guan Zhang, Gang Zhao, Peng Zhang, and Ying Li. Investigation on the sonocatalytic degradation of acid red b in the presence of nanometer TiO₂ catalysts and comparison of catalytic activities of anatase and rutile TiO₂ powders. *Ultrasonics sonochemistry*, 14(5):545–551, 2007.
- [77] Virendra Kumar Saharan, Mandar P Badve, and Aniruddha B Pandit. Degradation of reactive red 120 dye using hydrodynamic cavitation. *Chemical Engineering Journal*, 178:100–107, 2011.
- [78] Marta Mrowetz, Carlo Pirola, and Elena Selli. Degradation of organic water pollutants through sonophotocatalysis in the presence of TiO₂. *Ultrasonics sonochemistry*, 10(4-5):247–254, 2003.
- [79] Uduak G Akpan and Bassim H Hameed. Parameters affecting the photocatalytic degradation of dyes using TiO₂-based photocatalysts: a review. *Journal of hazardous materials*, 170(2-3):520–529, 2009.
- [80] Jun Lin, Xingwang Zhang, Zhongjian Li, and Lecheng Lei. Biodegradation of reactive blue 13 in a two-stage anaerobic/aerobic fluidized beds system with a pseudomonas sp. isolate. *Bioresource technology*, 101(1):34–40, 2010.
- [81] Sunil Rajoriya, Swapnil Bargole, and Virendra Kumar Saharan. Degradation of reactive blue 13 using hydrodynamic cavitation: Effect of geometrical parameters and different oxidizing additives. *Ultrasonics sonochemistry*, 37:192–202, 2017.
- [82] Parag R Gogate and Pankaj N Patil. Combined treatment technology based on synergism between hydrodynamic cavitation and advanced oxidation processes. *Ultrasonics sonochemistry*, 25:60–69, 2015.
- [83] Elisabetta Petrucci, Luca Di Palma, Elena De Luca, and Giulia Massini. Biocides electrogeneration for a zero-reagent on board disinfection of ballast water. *Journal of applied electrochemistry*, 43(2):237–244, 2013.
- [84] Nahui Zhang, Zhitao Zhang, Mindong Bai, Cao Chen, Xiangying Meng, and Yiping Tian. Evaluation of the ecotoxicity and biological efficacy of ship's ballast water treatment based on hydroxyl radicals technique. *Marine pollution bulletin*, 64(12):2742–2748, 2012.
- [85] Zhilin Wu, Haifeng Shen, Bernd Ondruschka, Yongchun Zhang, Weimin Wang, and David H Bremner. Removal of blue-green algae using the hybrid method of hydrodynamic cavitation and ozonation. *Journal of hazardous materials*, 235:152–158, 2012.

- [86] Marylia Duarte Batista, Ana Carolina Borella Marfil Anhê, and Julio Cesar de Souza Inácio Gonçalves. Use of hydrodynamic cavitation for algae removal: effect on the inactivation of microalgae belonging to genus *scenedesmus*. *Water, Air, & Soil Pollution*, 228(11):443, 2017.
- [87] E.A. Solutions. *Fundamentals of orifice meter measurement*. White Paper, 2017.
- [88] Stephen J Kline. Describing uncertainty in single sample experiments. *Mech. Engineering*, 75:3–8, 1953.
- [89] VP Skripov. 1974, metastable liquids, john wiley & sons, new york.
- [90] E Brennen. Cavitation and bubble dynamics christopher. *California-New York: California Institute of Technology Pasadena*, 1995.
- [91] B Ward and DC Emmony. The energies and pressures of acoustic transients associated with optical cavitation in water. *Journal of modern optics*, 37(4):803–811, 1990.
- [92] R Pecha and B Gompf. Microimplosions: cavitation collapse and shock wave emission on a nanosecond time scale. *Physical review letters*, 84(6):1328, 2000.
- [93] Anna J Svagan, Jan-Willem Benjamins, Zeinab Al-Ansari, Daniel Bar Shalom, Anette Müllertz, Lars Wågberg, and Korbinian Löbmann. Solid cellulose nanofiber based foams—towards facile design of sustained drug delivery systems. *Journal of Controlled Release*, 244:74–82, 2016.
- [94] Athanasia E Christakou, Mathias Ohlin, Björn Önfelt, and Martin Wiklund. Ultrasonic three-dimensional on-chip cell culture for dynamic studies of tumor immune surveillance by natural killer cells. *Lab on a Chip*, 15(15):3222–3231, 2015.
- [95] Jack J Yoh, Hun-jae Jang, Mi-ae Park, Tae-hee Han, and Jung-moo Hah. A bio-ballistic micro-jet for drug injection into animal skin using a nd: Yag laser. *Shock Waves*, 26(1):39–43, 2016.
- [96] MQ Jiang, XQ Wu, YP Wei, G Wilde, and LH Dai. Cavitation bubble dynamics during pulsed laser ablation of a metallic glass in water. *Extreme Mechanics Letters*, 11:24–29, 2017.
- [97] Jean-Pierre Franc and Jean-Marie Michel. *Fundamentals of cavitation*, volume 76. Springer science & Business media, 2006.
- [98] Aijun Zhou, Qiang Fu, Wenhua Zhang, Bin Yang, Jingze Li, Pawel Ziolkowski, Eckhard Mueller, and Dongyan Xu. Enhancing the thermoelectric properties of the electroplated bi_2te_3 films by tuning the pulse off-to-on ratio. *Electrochimica Acta*, 178:217–224, 2015.
- [99] Mac J Smith, RJ Knight, and CW Spencer. Properties of $\text{bi}_2\text{te}_3\text{-sb}_2\text{te}_3$ alloys. *Journal of Applied Physics*, 33(7):2186–2190, 1962.

- [100] Seok Hwan Oh, Kwang-Cheol Lee, Jaechul Chun, Moohwan Kim, and Seung S Lee. Micro heat flux sensor using copper electroplating in su-8 microstructures. *Journal of Micromechanics and Microengineering*, 11(3):221, 2001.